Contrib Mineral Petrol (2002) 143: 38–55
DOI 10.1007/s00410-001-0330-9

Jay J. Ague

Gradients in fluid composition across metacarbonate layers of the Wepawaug Schist, Connecticut, USA

Received: 11 June 2001 / Accepted: 17 October 2001 / Published online: 10 January 2002

Abstract Metamorphic index mineral zones, pressure–temperature (P–T) conditions, and CO_2–H_2O fluid compositions were determined for metacarbonate layers within the Wepawaug Schist, Connecticut, USA. Peak metamorphic conditions were attained in the Acadian orogeny and increase from ~420 °C and ~6.5 kb in the low-grade greenschist facies to ~610 °C and ~9.5 kb in the amphibolite facies. The index minerals oligoclase, biotite, calcic amphibole, and diopside formed with progressive increases in metamorphic intensity. In the upper greenschist facies and in the amphibolite facies, prograde reaction progress is greatest along the margins of metacarbonate layers in contact with surrounding schists, or in reaction selvages bordering syn-metamorphic quartz veins. New index minerals typically appear first in these more highly reacted contact and selvage zones. It has been postulated that this spatial zonation of mineral assemblages resulted from infiltration, largely by diffusion, of water-rich fluids across lithologic contacts or away from fluid conduits like fractures. In this model, the infiltrating fluids drove prograde CO_2 loss and were derived from surrounding dehydrating schists or sources external to the metasedimentary sequence. The model predicts that significant gradients in the mole fraction of CO_2 (X_{CO_2}) should have been present during metamorphism, but new estimates of fluid composition indicate that differences in X_{CO_2} preserved across layers or vein selvages were very small, ~0.02 or less. However, analytical solutions to the two-dimensional advection–dispersion-reaction equation show that only small fluid composition gradients across layers or selvages are needed to drive prograde CO_2 loss by diffusion and mechanical dispersion. These gradients, although typically too small to be measured by field-based techniques, would still be large enough to dominate the effects of fluid flow and reaction along regional T and P gradients. Larger gradients in fluid composition may have existed across some layers during metamorphism, but large gradients favor rapid reaction and would, therefore, seldom be preserved in the rock record. Most of the H_2O needed to drive prograde CO_2 loss probably came from regional dehydration of surrounding metapelitic schists, although H_2O-rich diopside zone conditions may have also required an external fluid component derived from syn-metamorphic intrusions or the metavolcanic rocks that structurally underlie the Wepawaug Schist.

J.J. Ague
Department of Geology and Geophysics,
Yale University, P.O. Box 208109,
New Haven, CT 06520-8109, USA
E-mail: jay.ague@yale.edu
Tel.: +1-203-4323171
Fax: +1-203-4323134

Editorial responsibility: T.L. Grove

Introduction

Devolatilization of metasedimentary sequences is a basic result of regional metamorphism and plays a fundamental role in the cycling of volatiles through the Earth's crust. Metacarbonate rocks are the source of most of the CO_2 evolved by regional metamorphism, but considerable uncertainty remains regarding the processes of fluid release and transport. Devolatilization, resulting from heating and fluid flow during dynamic regional metamorphism, depends critically on both local and regional gradients in fluid composition (cf. Ague 2000). For example, gradients in fluid composition that arise as fluids flow and react along regional gradients in temperature (T) and pressure (P) may drive devolatilization (e.g., Baumgartner and Ferry 1991; Ferry 1992, 1994; Léger and Ferry 1993). Local gradients, on the other hand, may arise between intercalated layers, each of which evolves a different fluid composition during prograde heating in a flow field (e.g., Hewitt 1973; Ague and Rye 1999; Ague 2000). Exchange of volatile species between layers caused by diffusion through the fluid phase, dispersion, and advection may then drive coupled devolatilization reactions (cf. Ague 2000). Furthermore, fluids

that are out of chemical and isotopic equilibrium with their metasedimentary surroundings, such as those released from crystallizing intrusions, will create gradients in fluid composition and promote reactions in and around the conduits through which they flow (e.g., fractures or permeable layers; cf. Tracy et al. 1983; Palin 1992; Ague and Rye 1999). There is no doubt that the local and regional scale gradients discussed above are fundamental to devolatilization of the Earth's crust, but their relative roles in regional metamorphism are still controversial. Consequently, in this study, local and regional scale variations in fluid compositions recorded by metacarbonate layers during Barrovian-style metamorphism of the Wepawaug Schist, Connecticut, are investigated in order to constrain processes of volatile release and transport in a common type of regional metamorphic setting.

Regional overview

The Wepawaug Schist is dominated by metapelitic rocks, but includes lesser amounts of metapsammitic and metacarbonate layers. The metacarbonate layers range from a few centimeters to 10 m thick (most are $\sim$ 1 m thick) and are widely spaced in outcrop. The overall volume of metacarbonate rock across the Schist is difficult to estimate because of exposure limitations, but is probably in the range of 1–10%. Locally, however, metacarbonate abundance can reach several 10's of percent in some outcrops. Metamorphism occurred during the Acadian orogeny ($\sim$420–380 Ma; Lanzirotti and Hanson 1996).

Metamorphic grade increases from the Barrovian chlorite zone in the east to the kyanite zone in the west (Fig. 1). Chlorite and muscovite broke down to simultaneously produce biotite and garnet in metapelitic rocks (van Haren et al. 1996; Ague 2000). Biotite is typically the first mineral to appear upgrade of the chlorite zone in hand samples, but, in thin section, it is usually accompanied by microscopic to $\sim$1 mm diameter garnets. Consequently, the metamorphic map of Fig. 1A is simplified relative to earlier maps (e.g., Fritts 1965; Ague 1994) by combining biotite and garnet index minerals into a single "biotite–garnet" (Bt–Grt) zone. Similarly, the first appearance of macroscopic staurolite is also often accompanied by microscopic kyanite, so the amphibolite facies is mapped simply as the "staurolite–kyanite" (St–Ky) zone (Fig. 1A). In both zones, index mineral grain size increases markedly to the west such that the metapelitic rocks in the western biotite–garnet zone contain abundant, large ($\sim$0.25–1 cm scale) garnets, and the western staurolite–kyanite zone contains kyanite porphyroblasts of similar size.

The central part of the staurolite–kyanite zone was intruded by dikes, pods, and lenses of felsic igneous rock mapped by Fritts (1965) as "Woodbridge Granite" and "Devonian Pegmatite". The rocks are tonalitic to

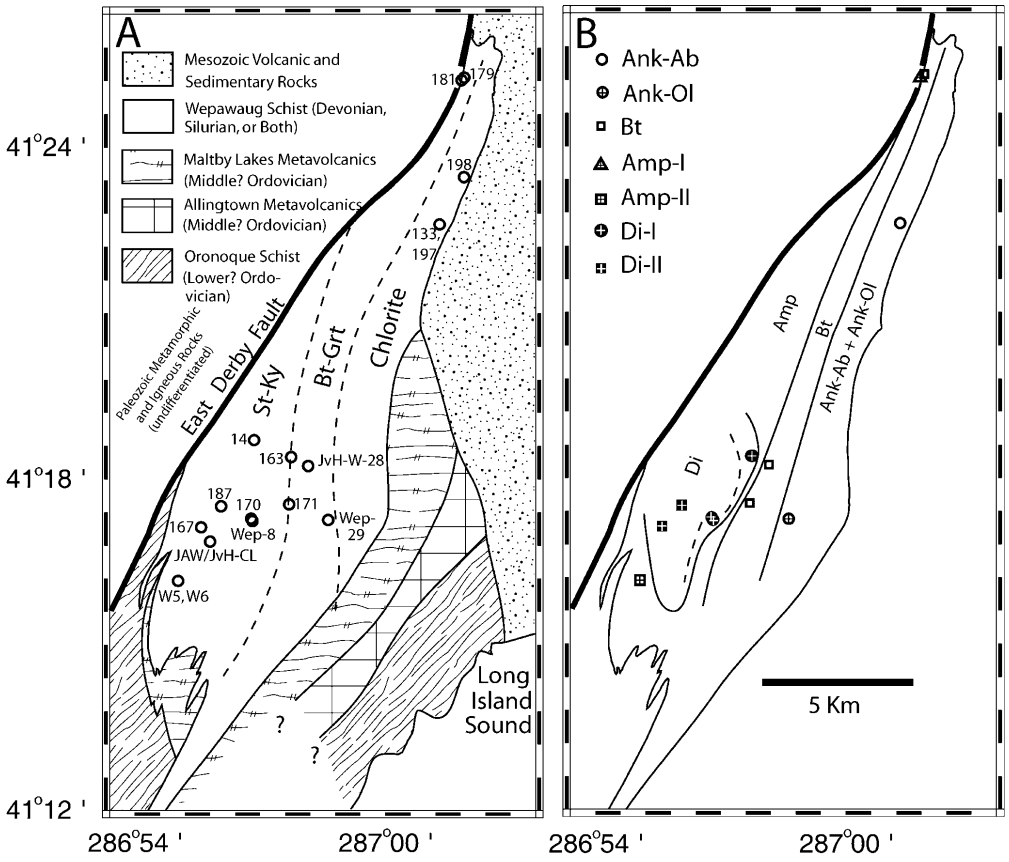

Fig. 1A,B. Geologic maps of the Wepawaug Schist. **A** Generalized geological relations from Fritts (1965). Metapelitic index mineral zones modified from Ague (1994): *Chlorite* Chlorite zone; *Bt–Grt* biotite–garnet zone; *St–Ky* staurolite–kyanite zone. All sample locality numbers begin with JAW unless otherwise noted. **B** Metacarbonate mineral zones mapped as part of this study. *Ank–Ab* Ankerite–albite; *Ank–Ol* ankerite–oligoclase; *Bt* biotite; *Amp-I* amphibole-I; *Amp-II* amphibole-II; *Di-I* diopside-I; *Di-II* diopside II

granitic in composition, comprise quartz + plagioclase + muscovite ± K-feldspar ± garnet ± biotite, and, on the basis of field and petrographic relationships, were broadly contemporaneous with metamorphism (Ague 1994). The ''Woodbridge Granite'' mapped by Fritts (1965) in the greenschist facies differs from that in the amphibolite facies, and comprises pre-metamorphic felsic tuffs and, possibly, very shallow level intrusive dikes (Bahr 1976; Ague 1994).

Mineral assemblages and lithologic contacts

Fritts (1965) and Hewitt (1973) were the first to document progressive changes in metacarbonate mineral assemblages with increasing metamorphic grade in the Schist, but they did not map out the regional distribution of assemblages. The new map made for the present study is shown in Fig. 1B, and is based on field and petrographic examination of several hundred outcrops. Mineral zone terminology is based on Ferry (1992) unless otherwise noted, and mineral assemblages are given in Table 1. The mineral reaction summaries below follow Hewitt (1973), Tracy et al. (1983), Ferry (1992), Palin (1992), and Ague and van Haren (1996).

At the lowest metamorphic grade, the principal assemblage in metacarbonate layers is Cc + Ank + Qtz + Ms + Ab + Py + Rt (ankerite–albite, or Ank–Ab zone). In northern New England (Ferry 1992, 1994; Léger and Ferry 1993), paragonite is fairly common, and breaks down with increasing grade to form plagioclase according to the generalized reaction 1 in Table 2, giving rise the ankerite–oligoclase (Ank–Ol) zone. Paragonite has not been observed in the Wepawaug Schist, but one sample (Wep-29a) in the Barrovian (metapelitic) biotite–garnet zone contains abundant oligoclase, strongly

Table 1. Prograde carbonate, silicate, and oxide mineral assemblages; trace phases not listed. Index mineral zones: *Ank–Ab* Ankerite–albite; *Ank–Ol* ankerite–oligoclase; *Bt* biotite; *Amp-I* amphibole-I; *Amp-II* amphibole-II; *Di-I* diopside-I; *Di-II* diopside-II. Rock type: *C* Contact between metacarbonate and metapelite; *DZ-CS* diopside–zoisite calc-silicate; *HC-CS* hornblende–clinozoisite calc-silicate; *HG-CS* hornblende–garnet calc-silicate; *IML* interior of metacarbonate layer; *MML* margin of metacarbonate layer; *V* vein; *VS* vein selvage; *VSC* vein selvage; vein runs along lithologic contact between metapelite and metacarbonate. *Amp* amphibole, other mineral abbreviations after Kretz (1983): *Cc* calcite; *Ank* ankerite; *Ms* muscovite; *Chl* chlorite; *Pl* plagioclase; *Qtz* quartz; *Bt* biotite; *Czo* clinozoisite; *Zo* zoisite; *Kfs* K-feldspar; *Grt* garnet; *Di* diopside; *Rt* rutile; *Ttn* titanite. The last digit in some sample numbers (e.g., the –2 at the end of JAW-197A-2) denotes the specific thin section investigated

Sample	Zone	Type	Cc	Qtz	Ank	Ms	Chl	Pl	Bt	Czo/Zo	Kfs	Amp	Grt	Di	Rt	Ttn
JAW-197A-2	Ank–Ab	IML	X	X	X	X		X							X	
JAW-197A-3	Ank–Ab	VS	X	X	X	X	X	X							X	
Wep-29a	Ank–Ol	IML	X	X	X	X		X							X	
JAW-171A	Bt	C	X	X	X	X		X	X	Czo					X	
JAW-179B	Bt	IML	X	X				X	X	Czo					X	
JAW-179H	Bt	V	X	X				X	X	Czo					X	X
JvH-W-28-1	Bt	VSC	X	X	X	X		X	X	Czo					X	
JvH-W-28-3	Bt	IML	X	X	X	X		X	X						X	
JvH-W-28-4	Bt	VSC	X	X	X	X		X	X	Czo					X	
JAW-181B-2	Amp-I	MML[a]	X	X					X	Czo	X	X				X
JAW-181F-3	Amp-I	IML	X	X				X	X	Czo						X
JAW-181FF-2	Amp-I	VS	X	X				X	X	Czo	X	X				X
JAW-181H-1	Amp-I	HC-CS	X	X						Czo	X	X	X			X
JAW-181SI	Amp-I	HC-CS	X	X						Czo		X	X			X
W5	Amp-II	IML	X	X				X	X	Czo		X	X			X
W6A[b]	Amp-II	C	X	X				X		Czo		X	X			X
JAW-163IR	Di-I	DZ-CS	X	X						Zo		X		X		X
JAW-163IX	Di-I	IML	X	X					X	Zo		X[c]		X		X
JAW-163IIIH	Di-I	IML	X	X					X	Zo	X	X				X
JAW-163IVA	Di-I	IML	X	X					X	Zo		X		X		X
JAW-170A	Di-I	IML	X	X					X	Czo	X	X				X
JAW-170C	Di-I	DZ-CS	X	X					X[d]	Zo		X		X		X
Wep-8a	Di-I	IML	X	X				X	X			X				X
Wep-8b	Di-I	DZ-CS	X	X						Zo		X[c]		X		X
JAW-14-2	Di-II	HG-CS		X				X	X[e]			X	X		X[e]	
JAW-167A	Di-II	IML	X	X						Zo		X		X		X
JAW-167D	Di-II	MML[f]	X	X						Zo		X		X		X
JAW-187A-2	Di-II	DZ-CS	X	X						Zo		X	X	X		X
JAW-187M-1	Di-II	IML	X	X						Zo		X		X		X
JAW-187N-3	Di-II	DZ-CS	X	X						Zo		X		X		X

[a]Margin of metacarbonate layer at contact with hornblende–clinozoisite calc-silicate
[b]Some relic biotite included within hornblende
[c]Possible retrograde replacement of diopside
[d]Small amount of biotite (< 1 vol%) present; heavily chloritized and intergrown with traces of K-feldspar
[e]Biotite rare and chloritized; rutile rimmed by some retrograde ilmenite
[f]Margin of metacarbonate layer at contact with diopside–zoisite calc-silicate

Table 2. Reactions used to estimate *P*, *T*, and X_{CO_2}. *Ab* albite, *Alm* almandine, *An* anorthite, *Ann* annite, *Dol* dolomite, *Fac* ferroactinolite, *Fts* ferrotschermakite, *Grs* grossular, *Hd* hedenbergite, *Ky* kyanite, *Pg* paragonite, *Phl* phlogopite, *Prp* pyrope, *Tr* tremolite, *Ts* tschermakite; other abbreviations defined in Table 1

	Reaction
1	$Cal + Pg + 2\ Qtz = Ab + An + H_2O + CO_2$
2	$3\ Qtz + Pg + 5\ Dol + 3\ H_2O = Ab + 5\ Cal + Chl + 5\ CO_2$
3	$3\ Dol + Ms + 2\ Qtz = Phl + 2\ Cal + An + 4\ CO_2$
4	$Rt + Qtz + Cc = Ttn + CO_2$
5	$Cal + 3\ An + H_2O = 2\ Zo/Czo + CO_2$
6	$5\ Cal + 3\ Qtz + 2\ Zo/Czo = 3\ Grs + H_2O + 5\ CO_2$
7	$6\ Cal + 5\ Phl + 24\ Qtz = 3\ Tr + 5\ Kfs + 2\ H_2O + 6\ CO_2$
8	$5\ Dol + 8\ Qtz + H_2O = 3\ Cal + Tr + 7\ CO_2$
9	$21\ Cal + 5\ Prp + 24\ Qtz + 3\ H_2O = 3\ Tr + 5\ Grs + 21\ CO_2$
10	$3\ Cal + Phl + 6\ Qtz = Kfs + 3\ Di + H_2O + 3\ CO_2$
11	$3\ Cal + Tr + 2\ Qtz = 5\ Di + H_2O + 3\ CO_2$
12	$Di + Alm = Hd + Prp$
13	$Phl + Alm = Ann + Prp$
14	$Ms + Grs + Py = Phl + 3\ An$
15	$Grs + 2\ Ky + Qtz = 3\ An$
16	$6\ An + 3\ Tr = 2\ Grs + Prp + 3\ Ts + 6\ Qtz$
17	$6\ An + 3\ Fac = 2\ Grs + Alm + 3\ Fts + 6\ Qtz$

suggesting that paragonite was present in the lower-grade protolith. With further increases in grade, biotite and more calcic plagioclase formed by the breakdown of Ms and Ank, producing the biotite zone (e.g., model reaction 3; Table 2). Chlorite is rare in the biotite zone and its origin, whether prograde or retrograde, is generally difficult to ascertain.

A fundamental observation of Hewitt (1973) was that at biotite zone conditions and higher, the assemblages representing the greatest amount of devolatilization reaction progress are found (1) at the edges of the metacarbonate layers, at lithologic contacts with surrounding metaclastic schists, and (2) in reaction selvages adjacent to quartz veins (see the following section). The variations in reaction progress are generally subtle in the metacarbonate biotite zone. When present, they are manifested by increased amounts of Bt and/or the growth of clinozoisite at contacts with metapelite or quartz veins (e.g., model reaction 5, Table 2; Fig. 2A). At Ank–Ol and biotite zone conditions, variations in reaction progress across layers tend to be subdued or

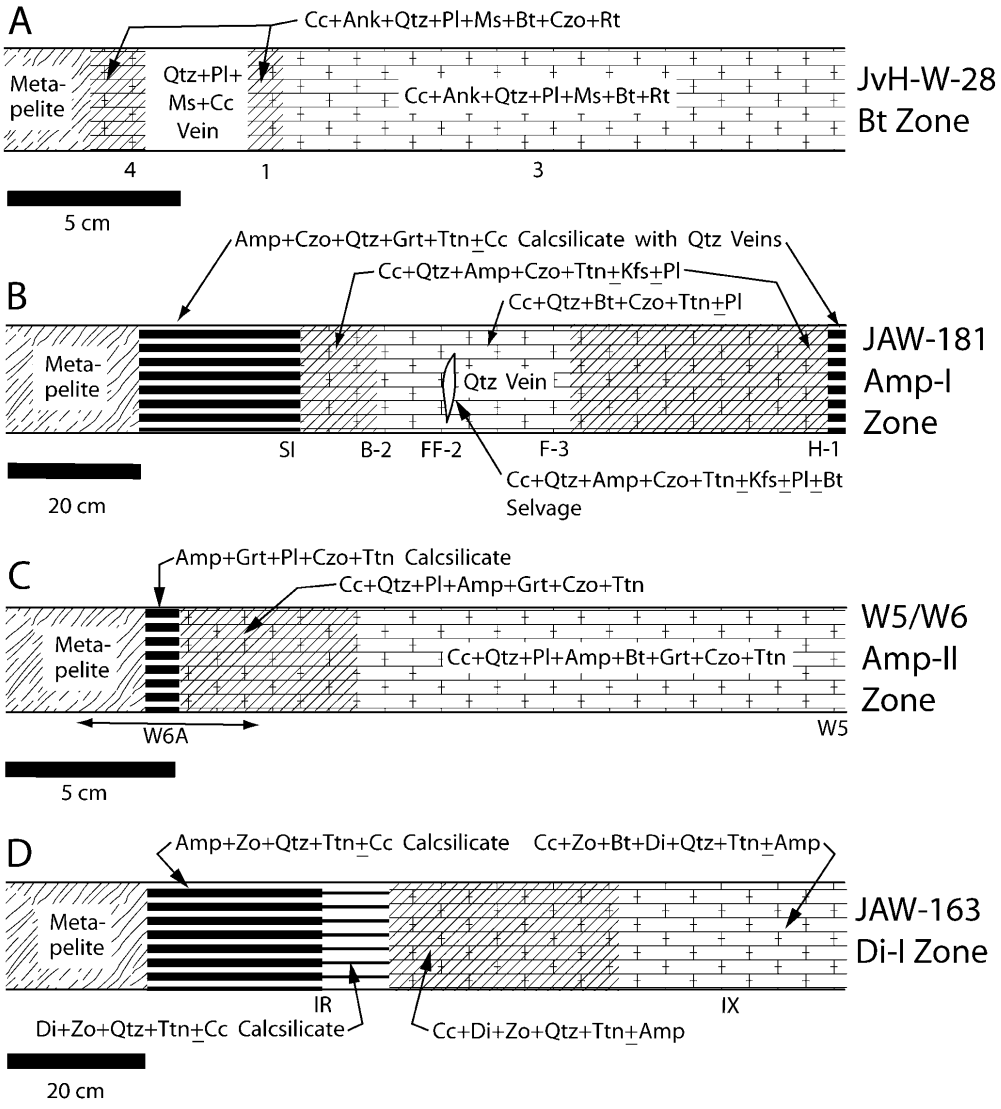

Fig. 2A–D. Profiles across metacarbonate layers perpendicular to lithologic contacts with metapelite layers or quartz veins showing spatial distribution of mineral assemblages for representative localities. Sample/thin section *numbers* shown along bottom of each profile. Note difference in scale between figures

"smeared out" mainly because of the solid solution in plagioclase and, relative to higher grades, somewhat slower rates of reaction (Ague and Rye 1999).

At higher grades, spatial variations in reaction progress become more extensive. Calcic amphibole is the next metacarbonate index mineral to form, and it grows by reactions such as reaction 8 (Table 2) in Ank-rich rocks, and at the expense of biotite in Ank-poor rocks. The amphibole zone is divided herein into two subzones on the basis of mineral assemblage. In the first (Amp-I), biotite-bearing, amphibole-absent assemblages persist in the interiors of layers, and amphibole has only grown in layer margins (Fig. 2B). With more reaction, a second zone is defined (Amp-II), in which amphibole is present throughout a given layer (Fig. 2C). Because of exposure limitations, these two zones are not distinguished on Fig. 1B. In both the Amp-I and Amp-II zones, the lithologic contacts themselves are occupied by strongly metasomatic calc-silicate rocks containing aluminous hornblende + Czo/Zo + Qtz + Ttn ± Grt ± Cc (Fig. 2B, C).

At the highest grades, Di forms at the expense of amphibole and/or biotite (e.g., model reactions 10, 11; Table 2). In the Di-I zone, assemblages that retain Amp ± Bt occupy layer interiors, whereas Di-rich assemblages are present at layer margins. In the Di-II zone, Di is present throughout the layers, Amp is absent or present in only small amounts, and Bt is absent. Zo, not Czo, coexists with Di in nearly all cases. Calc-silicates are most extensive in the diopside zones. A typical sequence of assemblages in the Di-I zone, from the center to the edge of a layer, is Amp ± Bt metacarbonate, to Di + Zo metacarbonate, to Di + Zo + Qtz + Ttn calc-silicate (little or no Cc), to Hbl + Zo + Qtz + Ttn ± Grt calc-silicate (Fig. 2D). Most of the Woodbridge Granite and Devonian Pegmatite intrusions are found in the Di-II zone.

Quartz veins

Systematic spatial variations in mineral assemblage are also present in reaction selvages adjacent to syn-metamorphic quartz veins (cf. Hewitt 1973; Tracy et al. 1983; Ague and Rye 1999). The veins are found along lithologic contacts between metacarbonate layers and surrounding schists, and cross cutting the metacarbonate layers. The sequences of mineral assemblages bordering veins in the biotite, amphibole, and diopside zones mimic those found at lithologic contacts, with the degree of reaction progress increasing as the veins are approached. Reaction selvages are the least abundant in the low-grade Ank–Ab zone, but one sample was found with a chlorite-bearing selvage surrounding a Cc–Ab vein (sample JAW-197A-3; Table 1). For those lithologic contacts that also contain quartz veins, it is probable that both vein-related and contact-related processes drove reaction progress and metasomatism.

Methods

Mineral chemistry

Mineral compositions (Tables 3, 4, 5, 6, 7, 8, 9, 10, 11, and 12) were determined using (1) wavelength-dispersive spectrometers on the fully automated JEOL JXA-8600 electron microprobe at Yale University; (2) a 15-kV accelerating voltage; (3) a defocused (5–10-μm diameter) beam; (4) natural and synthetic standards; (5) off-peak and fluorescence-corrected mean atomic number background corrections; and (6) ϕ–ρ–z matrix corrections. A 10-nA beam current was used for carbonate phases, a 20-nA beam for Grt, Czo/Zo, and Ttn, and a 15-nA beam for all other phases. Between 5 and 15 spot analyses on several grains of each mineral were done per thin section. Mineral composition systematics in metacarbonate layers were discussed in general by Hewitt (1973) and are extremely similar to those presented by Ferry (1992) for northern New England. Mineral energy-dispersive analyses and mapping as well as image processing were done with an EDAX Phoenix system mounted on the JXA-8600.

Pressure, temperature, and fluid composition

To maintain internal consistency with earlier studies (Ague 1994), the thermodynamic data base and recommended activity models of the Berman (1991) TWQ program were used for $P-T-X_{CO_2}$ calculations (X_{CO_2} = mole fraction CO_2 in fluid). The default models for pure H_2O and CO_2 fluid properties specified by the program were used, together with the mixing relations of Kerrick and Jacobs (1981). Reactions are given in Table 2. Data for some end-member solids modified by Berman and Aranovich (1996), as well as some provisional, unpublished data available at the TWQ website, are not internally consistent with the full Berman data set and were not used. T was also estimated using calcite–dolomite thermometry (Anovitz and Essene 1987) for rocks containing two coexisting carbonate phases (Table 3). The compositions of molecular fluids in the C–O–H–S system were computed following Ague et al. (2001).

Activity–composition relations for solids are given in Table 13. A variety of activity models have been advanced for tremolite (e.g., Blundy and Holland 1990; Kohn and Spear 1990; Léger and Ferry 1993; Mäder et al. 1994), but much uncertainty remains, particularly for $T < \sim 600$ °C. The simple model of Blundy and Holland (1990) for tremolite, which incorporates coupled A-site–Al^{iv} substitution, was modified by including a term for ideal mixing on the hydroxyl site (some amphiboles contain significant F). The model becomes more and more uncertain as Al content and departures from tremolite stoichiometry increase, so the highly aluminous amphiboles of sample JAW-181SI, which have a mole fraction of Al^{vi} of 0.47, were not used for fluid composition calculations (cf. Fig. 1 in Holland and Blundy 1994). Some amphiboles are chemically zoned (Table 8). For example, amphibole cores in sample JAW-163IIIH are more aluminous and Fe-rich than rims. On the other hand, cores of a few amphiboles in W-5 are less aluminous and more magnesian than rims, although most grains are relatively homogeneous. Rim compositions were used for the fluid composition calculations.

The metamorphic field temperature gradient (MFTG) and pressure gradient (MFPG) are based on Ague (1994), but are further constrained by new P and T estimates (Table 14). The focus herein is on peak P–T conditions, so retrograded staurolite–kyanite zone samples, which equilibrated at $T < 550$ °C and $P < 7$ kb (Ague 1994), are not considered. In addition, the P–T estimate from sample JAW-113D in Ague (1994) was updated by using the garnet composition at the Mn-minimum just inside the rim, and biotite composition far from garnet (e.g., Kohn and Spear 2000).

If T is known and two independent reactions are available, then the P and X_{CO_2} of equilibration can be estimated simultaneously by adjusting the P of the $T-X_{CO_2}$ diagram until the

Table 3. Calcite structural formulas based on three oxygens. All Fe as Fe^{2+}

Sample	Zone	Ca	Mg	Fe	Mn	Total[a]	T[b] (°C)
JAW-133[c]	Ank–Ab	0.956	0.020	0.016	0.007	99.75	385
JAW-168K	Ank–Ab	0.956	0.026	0.021	0.005	100.37	446
JAW-190B	Ank–Ab	0.968	0.021	0.013	0.003	100.22	393
JAW-197A-2	Ank–Ab	0.938	0.030	0.022	0.004	99.64	470
JAW-197A-3	Ank–Ab	0.951	0.024	0.023	0.007	100.23	441
Wep-19a[d]	Ank–Ol	0.928	0.048	0.018	0.007	–	536
Wep-29a	Ank–Ol	0.936	0.035	0.032	0.011	100.68	508
Wep-29c[d]	Ank–Ol	0.921	0.036	0.032	0.012	–	505
JAW-171A	Bt	0.891	0.055	0.034	0.011	99.53	578
JAW-179B	Bt	0.942	0.026	0.016	0.013	99.83	
JAW-179H	Bt	0.947	0.025	0.019	0.013	100.13	
JvH-W-28-1	Bt	0.904	0.054	0.030	0.009	99.87	570
JvH-W-28-3	Bt	0.918	0.049	0.023	0.007	99.80	549
JvH-W-28-4	Bt	0.889	0.052	0.030	0.017	99.40	572
JAW-181B-2	Amp-I	0.965	0.018	0.014	0.010	100.39	
JAW-181F-3	Amp-I	0.965	0.019	0.012	0.010	100.27	
JAW-181FF-2	Amp-I	0.964	0.018	0.013	0.007	100.09	
JAW-181H-1	Amp-I	0.959	0.019	0.013	0.012	100.10	
JAW-181SI	Amp-I	0.965	0.015	0.013	0.009	100.06	
W-5	Amp-II	0.936	0.024	0.017	0.013	99.49	
W-6A	Amp-II	0.955	0.018	0.013	0.012	99.86	
JAW-163IR	Di-I	0.977	0.004	0.003	0.007	99.46	
JAW-163IX	Di-I	0.984	0.004	0.002	0.006	99.83	
JAW-163IIIH	Di-I	0.980	0.008	0.004	0.006	99.83	
JAW-163IVA	Di-I	0.971	0.006	0.003	0.007	99.32	
JAW-170A	Di-I	0.981	0.008	0.003	0.005	99.86	
JAW-170C	Di-I	0.992	0.003	0.003	0.005	100.07	
Wep-8a	Di-I	0.966	0.018	0.008	0.009	100.01	
Wep-8b	Di-I	0.985	0.004	0.003	0.008	100.01	
JAW-167A	Di-II	0.977	0.005	0.004	0.006	99.57	
JAW-167D	Di-II	0.991	0.005	0.003	0.006	100.24	
JAW-187A-2	Di-II	0.983	0.004	0.005	0.008	99.91	
JAW-187M-1	Di-II	0.983	0.003	0.003	0.006	99.77	
JAW-187N-3	Di-II	0.978	0.003	0.003	0.006	99.49	

[a]Total weight percent computed assuming 1 mol CO_2 per mole of cations in matrix correction iterations
[b]Calcite–dolomite thermometry (Anovitz and Essene 1987)
[c]From Ague (1994)
[d]From Hewitt (1973)

Table 4. Ankerite structural formulas based on six oxygens. All Fe as Fe^{2+}

Sample	Zone	Ca	Mg	Fe	Mn	Total[a]
JAW-190B	Ank–Ab	1.013	0.835	0.161	0.010	100.46
JAW-197A-2	Ank–Ab	1.019	0.740	0.237	0.015	100.26
JAW-197A-3 (C)[b]	Ank–Ab	1.034	0.791	0.176	0.024	100.62
JAW-197A-3 (R)[b]	Ank–Ab	1.019	0.674	0.293	0.027	100.28
JAW-197A-3 (B)[b]	Ank–Ab	1.023	0.703	0.263	0.026	100.37
JAW-198A[c]	Ank–Ab	1.053	0.354	0.585	0.021	100.28
Wep-29a	Ank–Ol	1.017	0.699	0.266	0.033	100.36
JAW-171A	Bt	1.027	0.734	0.224	0.028	100.30
JvH-W-28-1	Bt	1.028	0.743	0.216	0.026	100.33
JvH-W-28-3	Bt	1.013	0.791	0.185	0.015	100.08
JvH-W-28-4	Bt	1.028	0.704	0.229	0.043	100.09

[a]Total weight percent computed assuming 1 mol CO_2 per mole of cations in matrix correction iterations
[b]*C* Core of grains; *R* rim; *B* bulk average composition
[c]Metatuff

reactions intersect at the known T. For three or more independent reactions, P, T, and X_{CO_2} can be estimated by adjusting P soas to optimize the convergence of all reactions to a single $T - X_{CO_2}$ region. These methods proved to be sensitive indicators of intensive variables (Fig. 3).

Uncertainties for X_{CO_2} calculations.

In order to assess gradients in fluid composition across the metacarbonate layers, uncertainties on calculated fluid compositions need to be understood. Random errors in electron microprobe analyses and natural variability in mineral compositions were

Table 5. Feldspar analyses. Mole fractions anorthite (*An*), albite (*Ab*), orthoclase (*Or*), and celsian (*Cs*) compounds. *Pl* plagioclase, *Kfs* K-feldspar

Sample	Phase	Zone	X_{An}	X_{Ab}	X_{Or}	X_{Cs}	Total
JAW-197A-2	Pl	Ank–Ab	0.020	0.976	0.003	–	99.79
JAW-197A-3	Pl	Ank–Ab	0.019	0.976	0.004	0.001	100.53
JAW-198A[a]	Pl	Ank–Ab	0.006	0.987	0.006	–	100.78
Wep-29a	Pl	Ank–Ol	0.177	0.818	0.004	0.001	100.60
AW-171A	Pl	Bt	0.521	0.476	0.003	–	100.17
JAW-179B	Pl	Bt	0.292	0.700	0.006	0.002	99.82
JAW-179H	Pl	Bt	0.292	0.702	0.005	0.001	100.14
JvH-W-28-1 (C)[b]	Pl	Bt	0.212	0.782	0.005	0.001	99.86
JvH-W-28-1 (R)[b]	Pl	Bt	0.379	0.616	0.004	0.001	99.52
JvH-W-28-3	Pl	Bt	0.420	0.569	0.011	–	99.79
JvH-W-28-4	Pl	Bt	0.407	0.583	0.004	0.002	99.45
JAW-181B-2	Kfs	Amp-I	–	0.010	0.985	0.005	99.69
JAW-181F-3	Pl	Amp-I	0.336	0.659	0.005	–	99.27
JAW-181FF-2	Pl	Amp-I	0.331	0.660	0.010	0.001	99.57
JAW-181FF-2	Kfs	Amp-I	–	0.009	0.987	0.004	100.00
W-5	Pl	Amp-II	0.862	0.132	0.004	0.002	100.25
W-6A	Pl	Amp-II	0.887	0.112	0.001	–	99.97
W-6A (C)[c]	Pl	Amp-II	0.272	0.725	0.003	–	99.86
W-6A (R)[c]	Pl	Amp-II	0.452	0.543	0.003	0.002	100.08
JAW-163IIIH	Kfs	Di-I	–	0.007	0.980	0.013	100.54
JAW-170A	Pl	Di-I	0.358	0.631	0.010	0.001	99.74
JAW-170A	Kfs	Di-I	–	0.071	0.908	0.021	100.20
JAW-170C	Kfs	Di-I	0.002	0.009	0.987	0.002	99.64
Wep-8a	Pl	Di-I	0.423	0.571	0.005	0.001	99.88
JAW-14-2	Pl	Di-II	0.280	0.711	0.008	0.001	100.29
JAW/JvH-CL[d]	Pl	Di-II	0.085	0.907	0.007	0.001	100.48

[a]Metatuff
[b]*C* core, *R* rim of plagioclase; rim composition used for fluid composition calculations
[c]*C* core, *R* rim of plagioclase in metapelite
[d]Granite

Table 6. Muscovite and chlorite structural formulas. Muscovite, cations per 11 oxygens (excluding H_2O); chlorite, cations per 14 oxygens (excluding H_2O). Oxygen equivalents of F, Cl not subtracted from weight percent totals. All Fe as Fe^{2+}

Sample	Phase	Zone	Si	Al^{iv}	Al^{vi}	Ti	Fe	Mg	Mn	Ba	Na	K	F	Cl	Total
JAW-197A-3	Chl	Ank–Ab	2.792	1.208	1.276	0.004	1.866	2.796	0.017	–	–	0.005	0.098	0.002	88.11
JAW-168Eii	Ms	Ank–Ab	3.210	0.790	1.744	0.028	0.079	0.193	0.002	0.006	0.070	0.818	0.071	0.001	96.27
JAW-168K	Ms	Ank–Ab	3.189	0.811	1.757	0.028	0.079	0.174	–	0.006	0.080	0.840	0.061	–	95.11
JAW-197A-2	Ms	Ank–Ab	3.196	0.804	1.755	0.026	0.078	0.177	0.001	0.006	0.075	0.838	0.063	–	95.15
JAW-197A-3	Ms	Ank–Ab	3.241	0.759	1.676	0.021	0.124	0.229	0.001	0.010	0.050	0.871	0.056	–	94.20
JAW-198A[a]	Ms	Ank–Ab	3.286	0.714	1.603	0.030	0.198	0.221	0.002	0.003	0.017	0.918	0.092	–	95.60
Wep-29a	Ms	Ank–Ol	3.164	0.836	1.802	0.025	0.071	0.128	0.002	0.006	0.099	0.818	0.033	–	95.79
JAW-171A	Ms	Bt	3.136	0.864	1.799	0.030	0.061	0.131	0.001	0.017	0.083	0.847	0.021	0.001	95.05
JvH-W-28-1	Ms	Bt	3.108	0.893	1.822	0.017	0.069	0.128	–	0.021	0.097	0.828	0.013	–	94.92
JvH-W-28-3	Ms	Bt	3.124	0.876	1.805	0.025	0.053	0.141	0.001	0.026	0.088	0.835	0.023	–	95.59
JvH-W-28-4	Ms	Bt	3.111	0.889	1.810	0.030	0.065	0.117	–	0.022	0.122	0.810	0.017	–	95.11
JAW/JvH-CL[b]	Ms	Di-II	3.150	0.850	1.818	0.003	0.187	0.029	0.001	0.001	0.034	0.915	0.045	–	95.59

[a]Metatuff
[b]Granite

evaluated simultaneously using bootstrap error analysis (e.g., Efron and Tibshirani 1993; Ague and van Haren 1996). Consider one of the common reactions for estimating fluid compositions (reaction 5 in Table 2) and measured mineral compositions from representative sample JvH-W-28-4 at $P = 7.5$ kb (Table 14). Propagation of errors through the full fluid calculation, incorporating the TWQ thermodynamic data and the activity models of Table 13, indicates that $\pm 2\sigma$ uncertainties on X_{CO_2} average ± 0.011 for the likely T range of equilibration for this sample (520–560 °C). Results for other reactions and samples are comparable. The main conclusion is that the minimum difference in X_{CO_2} that is likely to be resolvable between samples is ~0.02.

If a large number of linearly independent reactions are available, then the uncertainties on X_{CO_2} can be estimated by the degree to which intersections among all reactions converge to a single $P - T - X_{CO_2}$ point (e.g., Berman 1991). For example, this type of analysis is possible for sample W-5 (four independent reactions; Fig. 3B). The INTERSX software of Berman (1991) calculates a "standard deviation" of ± 0.01 on X_{CO_2} based on the amount of scatter among intersections, although the relationship between this value and the "true" statistical confidence limits on X_{CO_2} is not straightforward or easily resolvable. Nonetheless, the magnitude of the uncertainty is comparable to that obtained by bootstrap analysis, reinforcing the conclusion that differences in X_{CO_2} between samples must be greater than ~0.02 to be detectable with the methods used here. It should be noted that for samples such as W-5, there is no guarantee that all the independent reactions and their associated dependent reactions will converge to a geologically

Table 7. Biotite structural formulas based on 11 oxygens (excluding H_2O). Oxygen equivalents of F, Cl not subtracted from weight percent totals. All Fe as Fe^{2+}

Sample	Zone	Si	Al^{iv}	Al^{vi}	Ti	Fe	Mg	Mn	Ba	Na	K	F	Cl	Total
JAW-171A	Bt	2.787	1.213	0.401	0.098	1.021	1.343	0.004	0.009	0.016	0.850	0.110	0.001	94.59
JAW-179B	Bt	2.810	1.191	0.389	0.089	0.939	1.455	0.012	0.005	0.010	0.834	0.100	0.001	95.99
JAW-179H	Bt	2.831	1.169	0.392	0.078	0.911	1.491	0.010	0.005	0.019	0.828	0.103	0.001	95.52
JvH-W-28-1	Bt	2.805	1.195	0.407	0.077	0.896	1.489	0.006	0.005	0.010	0.865	0.108	0.001	95.43
JvH-W-28-3	Bt	2.823	1.177	0.394	0.069	0.794	1.621	0.004	0.005	0.007	0.866	0.137	0.001	95.74
JvH-W-28-4	Bt	2.808	1.192	0.370	0.088	0.966	1.451	0.009	0.004	0.013	0.856	0.109	0.001	95.28
JAW-181B-2	Amp-I	2.835	1.165	0.349	0.062	0.944	1.543	0.010	0.008	0.017	0.843	0.208	0.001	96.79
JAW-181F-3	Amp-I	2.816	1.184	0.339	0.073	0.956	1.532	0.008	0.004	0.022	0.858	0.165	0.001	95.91
JAW-181FF-2	Amp-I	2.811	1.189	0.332	0.075	0.957	1.541	0.007	0.004	0.017	0.857	0.178	0.001	96.43
JAW-181SIV[a]	Amp-I	2.842	1.158	0.371	0.080	0.972	1.441	0.013	0.005	0.014	0.851	0.281	0.001	96.94
W-5	Amp-II	2.828	1.172	0.295	0.092	0.946	1.545	0.013	0.007	0.009	0.890	0.113	0.001	96.01
JAW-163IX	Di-I	2.893	1.107	0.246	0.042	0.719	1.908	0.020	0.010	0.004	0.884	0.311	–	97.28
JAW-163IIIH	Di-I	2.898	1.102	0.243	0.045	0.651	1.975	0.016	0.005	0.009	0.891	0.257	–	96.61
JAW-163IVA	Di-I	2.898	1.102	0.221	0.030	0.685	1.992	0.019	0.014	0.006	0.893	0.375	–	96.90
JAW-170A	Di-I	2.899	1.101	0.344	0.047	0.587	1.888	0.010	0.005	0.007	0.897	0.205	–	95.41
Wep-8a	Di-I	2.865	1.135	0.315	0.054	0.636	1.899	0.009	0.007	0.017	0.860	0.236	–	97.21
JAW/JvH-CL[b]	Di-II	2.723	1.277	0.519	0.056	2.122	0.149	0.016	–	0.008	0.913	0.073	0.004	96.44

[a]Metapelite
[b]Granite

reasonable $P-T-X_{CO_2}$ point. The fact that the reactions do converge is support for the internal consistency and applicability of the thermodynamic data and activity models.

Uncertainties on the thermodynamic data and activity models directly impact the uncertainties on absolute values of calculated fluid mole fractions, but the nature and amounts of the effects cannot be readily assessed. Errors are probably largest for Ank–Ab zone calculations owing to uncertainties on anorthite and paragonite component activities at low T. The relative differences, however, between metamorphic fluids present at contacts, in veins, or in metacarbonate layer interiors can be accurately estimated if the same reactions are used to evaluate fluid composition. Thus, the same reaction or set of reactions has been used whenever possible when evaluating a given outcrop. The absolute values of fluid mole fractions are also affected by uncertainties in T and P. Again, however, relative differences across a given layer can be estimated if P and T are constant– a reasonable assumption for the relatively thin layers studied here.

Pressure and temperature

The metamorphic field temperature gradient (MFTG) increases linearly, within error, from the eastern margin of the field area to about $x=0$ km (Fig. 4A). The best-fit line is: T (°C) $=-58.12x$ (km) $+577.10$; $r^2=0.950$. The best-fit line is based on all the T estimates and is taken to be the best estimate of the T to be used in fluid composition calculations for a given field site. Farther west in the amphibolite facies, no clear trend in T is evident. The average T is 609 °C (± 18 °C; 2σ) so, for simplicity, a T of 610 °C was assigned to this region and used in fluid composition calculations for most samples. The exceptions are three samples that have low variance mineral assemblages that permitted simultaneous constraint of P, T, and X_{CO_2} (samples W-5, W-6A, and JAW-187A-2).

The metamorphic field pressure gradient (MFPG) increases linearly, within error, from ~6.5 kb in the east to ~9.5 kb in the west (Fig. 4B). The best-fit line is: P (kb) $=-0.4933x$ (km) $+8.0913$; $r^2=0.84$. The MFPG incorporates P estimates from a diverse array of reactions (Table 14) and is considered more robust than the earlier version presented in Ague (1994). The phengite barometer (Massonne and Schreyer 1987) was also used to estimate minimum P for two low-grade samples containing coexisting muscovite and chlorite (Fig. 4). These minimum P estimates are consistent with the other results, but have large uncertainties and were not used in the MFPG fit.

Mole fractions of CO_2 and H_2O

Estimated fluid compositions follow two broad trends (Fig. 5). One is the systematic increase in X_{CO_2} with T defined by the Ank–Ab, Ank–Ol, biotite, and amphibole zones. This trend is controlled largely by the topologies of the major index mineral-forming reactions, which all tend to increase X_{CO_2} with prograde heating and reaction (cf. Léger and Ferry 1993; Ague and Rye 1999). In spite of uncertainties on anorthite and paragonite activities, $P-T-X_{CO_2}$ relations for the Ank–Ab zone samples are fully consistent with the presence of coexisting rutile and absence of titanite. The other trend is present only at the highest metamorphic grades ($T>575$ °C) and is defined by fluid compositions in the diopside zones. These compositions are significantly more water-rich than those of the other zones at high T conditions, as required by the topology of the Di-producing reactions (cf. Léger and Ferry 1993; Ague and Rye 1999).

Surprisingly, the calculations reveal no large differences in X_{CO_2} between the interiors of metacarbonate layers and the zones of greater reaction progress at lithologic contacts or in veins and vein selvages, regardless of rock bulk composition (Figs. 4C and 5).

Table 8. Calcic amphibole structural formulas based on 23 oxygens (excluding H_2O). Fe^{2+}, Fe^{3+} estimated using method of Holland and Blundy (1994). Oxygen equivalents of F, Cl not subtracted from weight percent totals

Sample	Zone	Si	Al^{iv}	Al^{vi}	Ti	Fe^{3+}	Fe^{2+}	Mg	Mn	Ca	Na	Na	K	F	Cl	Total
JAW-181B-2	Amp-I	6.825	1.175	0.730	0.028	0.209	1.447	2.495	0.051	1.938	0.062	0.221	0.104	0.139	–	97.70
JAW-181FF-2	Amp-I	6.822	1.178	0.626	0.032	0.371	1.360	2.571	0.043	1.881	0.117	0.159	0.076	0.161	0.003	98.05
JAW-181H-1	Amp-I	7.361	0.639	0.338	0.013	0.242	1.182	3.202	0.046	1.909	0.068	0.068	0.033	0.136	0.002	97.91
JAW-181SI	Amp-I	6.457	1.543	0.941	0.045	0.370	1.342	2.265	0.043	1.846	0.148	0.218	0.073	0.134	–	97.36
W-5(C)	Amp-II	7.304	0.696	0.403	0.020	0.211	1.131	3.224	0.057	1.890	0.064	0.064	0.040	0.077	–	97.93
W-5	Amp-II	6.679	1.321	0.686	0.040	0.438	1.010	2.762	0.065	1.886	0.114	0.120	0.112	0.091	–	97.94
W-6A	Amp-II	6.874	1.126	0.630	0.040	0.333	1.268	2.689	0.050	1.907	0.083	0.084	0.082	0.086	–	98.60
JAW-163IR	Di-I	7.232	0.768	0.385	0.020	0.292	1.040	3.189	0.058	1.911	0.090	0.113	0.060	0.176	–	98.26
JAW-163IX	Di-I	7.512	0.489	0.200	0.009	0.226	0.794	3.697	0.049	1.940	0.060	0.101	0.057	0.204	–	98.73
JAW-163IIIH (R)[a]	Di-I	7.664	0.336	0.279	0.006	0.067	0.804	3.719	0.044	1.980	0.020	0.117	0.043	0.159	–	98.94
JAW-163IIIH (C)[a]	Di-I	7.178	0.822	0.390	0.022	0.273	0.718	3.525	0.050	1.912	0.088	0.189	0.059	0.200	–	98.89
JAW-163IVA	Di-I	7.130	0.870	0.400	0.020	0.271	0.765	3.472	0.050	1.924	0.076	0.205	0.077	0.253	–	99.29
JAW-170A	Di-I	7.556	0.444	0.240	0.009	0.159	0.604	3.955	0.033	1.932	0.068	0.053	0.044	0.162	–	98.74
JAW-170C	Di-I	7.630	0.370	0.172	0.006	0.149	1.105	3.502	0.051	1.966	0.034	0.064	0.038	0.147	–	98.99
Wep-8a	Di-I	7.410	0.590	0.317	0.015	0.209	0.707	3.725	0.045	1.915	0.068	0.069	0.034	0.151	–	98.06
Wep-8b	Di-I	7.560	0.440	0.232	0.010	0.168	1.208	3.322	0.070	1.942	0.051	0.051	0.022	0.161	–	98.96
JAW-14-2	Di-II	6.450	1.550	0.985	0.049	0.457	1.123	2.386	0.031	1.764	0.205	0.152	0.063	0.051	–	97.07
JAW-167A	Di-II	7.527	0.474	0.176	0.007	0.240	0.866	3.632	0.052	1.950	0.050	0.105	0.043	0.200	–	98.95
JAW-167D	Di-II	7.539	0.461	0.171	0.009	0.229	0.917	3.583	0.055	1.964	0.036	0.117	0.036	0.206	–	98.51
JAW-187A-2	Di-II	7.684	0.316	0.139	0.004	0.141	1.321	3.325	0.070	1.964	0.036	0.042	0.027	0.204	–	98.49
JAW-187M-1	Di-II	7.575	0.425	0.145	0.008	0.248	1.214	3.290	0.058	1.970	0.030	0.106	0.016	0.167	–	98.33
JAW-187N-3	Di-II	7.666	0.334	0.174	0.004	0.120	1.318	3.319	0.070	1.960	0.036	0.036	0.031	0.139	–	98.91

[a] *C* core; *R* rim of grains

Differences in X_{CO_2} across the layers as recorded by the mineral assemblages must have been less than the minimum resolvable value of about 0.02.

Hewitt (1973; his Fig. 4) inferred a large gradient in fluid composition across a lithologic contact based on a sharp drop in the anorthite content of plagioclase from metacarbonate ($\sim An_{90}$) to metapelite ($\sim An_{30-40}$) in sample Wep-16c. Samples W5 and W6A of the present study are from the Wep-16c layer (Fig. 2C). Within several centimeters of the contact, the plagioclase in the schist is markedly zoned from cores of $\sim An_{25}$ to rims of $\sim An_{45}$ (sample W6A; Table 5). Similar zoning relations

Table 9. Garnet structural formulas based on 12 oxygens, with almandine (*Alm*), pyrope (*Py*), spessartine (*Sps*), and grossular (*Grs*) mole fractions. All Fe as Fe^{2+}

Sample	Zone	Si	Al^{iv}	Al^{vi}	Ti	Fe	Mg	Mn	Ca	Total	X_{Alm}	X_{Py}	X_{Sps}	X_{Grs}
JAW-181H-1	Amp-I	2.971	0.029	1.994	0.006	1.846	0.223	0.277	0.666	99.85	0.613	0.074	0.092	0.221
JAW-181SI	Amp-I	2.980	0.020	1.998	0.003	1.953	0.252	0.118	0.679	100.27	0.651	0.084	0.039	0.226
JAW-181SIV[a]	Amp-I	2.968	0.032	1.994	0.004	2.080	0.310	0.038	0.589	99.41	0.690	0.103	0.013	0.195
JAW-113D[a]	Amp-II	2.990	0.010	1.986	0.001	2.112	0.380	0.005	0.529	99.69	0.698	0.126	0.002	0.175
W-5	Amp-II	2.981	0.019	1.998	0.007	1.626	0.367	0.274	0.732	99.94	0.542	0.122	0.091	0.244
W-6A	Amp-II	2.975	0.025	1.990	0.006	1.597	0.379	0.295	0.744	99.95	0.530	0.126	0.098	0.247
JAW-14-2	Di-II	2.983	0.017	1.989	0.004	1.880	0.384	0.116	0.636	99.88	0.623	0.127	0.038	0.211
JAW-187 A-2	Di-II	2.975	0.025	1.984	0.006	1.021	0.156	0.456	1.392	100.57	0.338	0.052	0.151	0.460
JAW/JvH-CL[b]	Di-II	3.000	–	2.022	–	2.423	0.027	0.294	0.223	100.53	0.817	0.009	0.099	0.075

[a]Metapelite
[b]Granite

Table 10. Diopside structural formulas based on six oxygens. All Fe as Fe^{2+}

Sample	Zone	Si	Al^{iv}	Al^{vi}	Ti	Fe	Mg	Mn	Ca	Na	Total
JAW-163IR	Di-I	1.993	0.007	0.027	–	0.239	0.718	0.021	0.973	0.021	99.26
JAW-163IX	Di-I	1.988	0.012	0.030	0.001	0.184	0.764	0.017	0.982	0.023	99.61
JAW-163IVA	Di-I	1.983	0.017	0.024	0.001	0.201	0.752	0.018	0.991	0.018	99.50
JAW-170C	Di-I	1.989	0.011	0.034	0.001	0.239	0.716	0.015	0.969	0.027	99.62
Wep-8b	Di-I	1.991	0.009	0.019	0.001	0.264	0.693	0.022	0.987	0.015	99.90
JAW-167A	Di-II	1.983	0.017	0.051	0.001	0.208	0.725	0.014	0.966	0.032	99.60
JAW-167D	Di-II	1.981	0.019	0.047	0.001	0.222	0.720	0.015	0.964	0.034	99.95
JAW-187A-2	Di-II	1.995	0.005	0.025	0.001	0.277	0.680	0.022	0.975	0.015	99.44
JAW-187M-1	Di-II	1.991	0.009	0.023	–	0.267	0.678	0.023	0.993	0.018	99.21
JAW-187N-3	Di-II	1.994	0.006	0.021	0.001	0.285	0.674	0.022	0.981	0.016	99.32

Table 11. Clinozoisite (*Czo*) and zoisite (*Zo*) structural formulas based on 12.5 oxygens (excluding H_2O). All Fe as Fe^{3+}. *n.d.* Not determined

Sample	Phase	Zone	Si	Ti	Al	Fe^{3+}	Ce^{3+}	La^{3+}	Mg	Mn	Ca	Total
JAW-171A	Czo	Bt	3.024	0.007	2.667	0.287	0.030	0.007	0.013	0.013	1.922	97.30
JAW-179B	Czo	Bt	3.006	0.010	2.673	0.306	n.d.	n.d.	0.012	0.020	1.964	97.20
JAW-179H	Czo	Bt	3.010	0.009	2.664	0.309	n.d.	n.d.	0.006	0.017	1.978	97.87
JvH-W-28-1	Czo	Bt	2.998	0.009	2.674	0.301	n.d.	n.d.	0.012	0.016	1.993	97.56
JvH-W-28-4	Czo	Bt	3.005	0.017	2.697	0.265	n.d.	n.d.	0.013	0.018	1.977	97.05
JAW-181B-2	Czo	Amp-I	3.006	0.010	2.644	0.329	n.d.	n.d.	0.007	0.014	1.982	97.11
JAW-181F-3	Czo	Amp-I	3.009	0.010	2.651	0.315	n.d.	n.d.	0.007	0.012	1.987	97.05
JAW-181FF-2	Czo	Amp-I	3.014	0.016	2.652	0.313	n.d.	n.d.	0.008	0.012	1.968	97.47
JAW-181H-1	Czo	Amp-I	3.006	0.011	2.625	0.342	n.d.	n.d.	0.009	0.015	1.989	97.93
JAW-181SI	Czo	Amp-I	3.007	0.012	2.662	0.305	n.d.	n.d.	0.006	0.012	1.991	97.63
W-5	Czo	Amp-II	3.010	0.010	2.682	0.297	n.d.	n.d.	0.010	0.013	1.967	97.51
W-6A	Czo	Amp-II	3.016	0.014	2.664	0.297	n.d.	n.d.	0.009	0.014	1.977	98.48
JAW-163IR	Zo	Di-I	3.009	0.003	2.854	0.128	n.d.	n.d.	0.005	0.006	1.992	98.03
JAW-163IX	Zo	Di-I	3.002	0.006	2.888	0.099	n.d.	n.d.	0.006	0.005	1.991	97.66
JAW-163IVA	Zo	Di-I	3.010	0.002	2.892	0.092	n.d.	n.d.	0.005	0.004	1.988	97.56
JAW-170A	Zo	Di-I	3.008	0.005	2.905	0.069	n.d.	n.d.	0.008	0.004	1.999	97.53
JAW-170C	Zo	Di-I	3.011	0.002	2.854	0.119	n.d.	n.d.	0.010	0.004	1.998	97.57
Wep-8b	Zo	Di-I	3.008	0.003	2.853	0.130	n.d.	n.d.	0.004	0.005	1.995	98.09
JAW-187A-2	Zo	Di-II	3.015	0.003	2.841	0.124	n.d.	n.d.	0.004	0.007	2.003	97.87
JAW-187M-1	Zo	Di-II	3.000	0.002	2.868	0.119	n.d.	n.d.	0.003	0.003	2.009	97.80
JAW-187N-3	Zo	Di-II	3.012	0.002	2.857	0.127	n.d.	n.d.	0.002	0.004	1.990	98.53

have been observed in metapelites at other contacts, and probably resulted from input of Ca from the metacarbonate layers into the metapelites during metamorphism. The change in anorthite content from metacarbonate to metapelite need not indicate a large change in X_{CO_2} because the mineral assemblages in the two layers are vastly different. Unfortunately, the assemblage of Qtz + Pl + Bt ± Grt in the metapelite is poorly suited for estimation of fluid composition. It is worth noting, however, that because of non-ideality in plagioclase, the activity of anorthite in metapelite (~0.89; W6A Pl rims) and metacarbonate (~0.85; W6A) layers is nearly the same. Thus, although there is a marked shift in anorthite mole fraction, gradients in anorthite activity, if present, were small. The two feldspar compositions may be separated by a solvus (cf. Smith and Brown 1988), in which case the activities of both anorthite and albite would have been the same across the contact.

Tracy et al. (1983) inferred large changes in X_{CO_2} of ~0.05 across a reaction zone adjacent to quartz veins at the Wep-8 sample locality based in part on the X_{CO_2} predicted by reaction 7 (Table 2) for the interior of the layer far-removed from the veins. Backscattered electron

Table 12. Representative rutile (*Rt*) and titanite (*Ttn*) structural formulas. Rutile formulas based on eight oxygens, titanite formulas based on 1 Si (cf. Deer et al. 1992). All Fe as Fe^{3+} in rutile and as Fe^{2+} in titanite. *n.d.* Not determined

Sample	Phase	Zone	Si	Ti	Al	Fe	Nb^{5+}	Ta^{5+}	Mg	Mn	Ca	Total
JAW-179H	Rt	Bt	–	3.907	0.003	0.057	0.035	0.001	–	0.001	0.004	99.73
JAW-179H	Ttn	Bt	1.000	0.891	0.077	0.005	0.009	0.002	–	0.002	0.985	100.17
JAW-181F-3	Ttn	Amp-I	1.000	0.902	0.067	0.007	n.d.	n.d.	–	0.002	0.992	99.68
JAW-181H-1	Ttn	Amp-I	1.000	0.879	0.091	0.009	n.d.	n.d.	0.001	0.002	0.987	99.38
W-6A	Ttn	Amp-II	1.000	0.904	0.074	0.007	n.d.	n.d.	–	0.002	0.989	99.80
Wep-8a	Ttn	Di-I	1.000	0.872	0.102	0.008	n.d.	n.d.	–	0.002	0.986	99.67
Wep-8b	Ttn	Di-I	1.000	0.852	0.118	0.006	n.d.	n.d.	–	0.002	0.984	99.63
JAW-187A-2	Ttn	Di-II	1.000	0.903	0.069	0.005	n.d.	n.d.	–	0.002	0.988	99.88
JAW-187M-1	Ttn	Di-II	1.000	0.801	0.176	0.006	n.d.	n.d.	–	0.002	1.000	99.28

Table 13. Activity–composition relations

	Abbreviation	Activity–composition relation	Notes
Amphibole	Amp	$a_{Ca_2Mg_5Si_8O_{22}(OH)_2,Amp} = (X_{Ca,M4})^2(X_{Mg,M13})^3 (X_{Mg,M2})^2(X_{Si,T1})^4(X_{OH})^2$	$X_{Ca,M4}$ = mole fraction Ca on M4 site $X_{Mg,M13}$ = mole fraction Mg on M1, M3 sites $X_{Mg,M2}$ = mole fraction Mg on M2 site $X_{Si,T1}$ = mole fraction Si on T1 site X_{OH} = mole fraction OH on hydroxyl site From Blundy and Holland (1990), modified to include mixing on hydroxyl site
Biotite	Bt	McMullin et al. (1991)	$X_{K,Bt}$ = K atoms per 11 oxygens
Calcite	Cc	$a_{CaCO_3,Cc} = X_{CaCO_3,Cc}$	$X_{CaCO_3,Cc}$ = Ca/ (Ca + Mg + Fe + Mn)
Chlorite	Chl	$a_{(Mg)_4(Mg,Al)(Al,Si)(Si)_6(OH)_8,Chl} = 16(X_{Mg,M1})^4 (X_{Mg,M2})(X_{Al,M2})(X_{Al,T2})(X_{Si,T2})(X_{OH})^8$	$X_{Mg,M1}$ = mole fraction Mg on M1 site $X_{Mg,M2}$ = mole fraction Mg on M2 site $X_{Al,M2}$ = mole fraction Al on M2 site $X_{Al,T2}$ = mole fraction Al on T2 site $X_{Si,T2}$ = mole fraction Si on T2 site X_{OH} = mole fraction OH on hydroxyl site From Holland and Powell (1990), modified to include mixing on hydroxyl site
Clinozoisite/Zoisite	Czo/Zo	$a_{Ca_2Al_3Si_3O_{12}(OH),Czo/Zo} = (Ca/2)^2(Al-2)$	If Ca > 2, set (Ca/2) = 1
Diopside	Di	$a_{CaMgSi_2O_6,Di} = X_{Ca,M2}X_{Mg,M1}$	$X_{Ca,M2}$ = mole fraction Ca on M2 site $X_{Mg,M1}$ = mole fraction Mg on M1 site
Dolomite	Dol	$a_{CaMg(CO_3)_2,Dol}$ = Mg atoms per six oxygens	
K-feldspar	Kfs	$a_{KAlSi_3O_8,Kfs} = X_{KAlSi_3O_8,Kfs}$	$X_{KAlSi_3O_8,Kfs}$ = K/(K + Na + Ca + Ba)
Garnet	Grt	Berman (1990)	
Hedenbergite	Hd	$a_{CaFeSi_2O_6,Di} = X_{Ca,M2}X_{Fe,M1}$	$X_{Ca,M2}$ = mole fraction Ca on M2 site $X_{Fe,M1}$ = mole fraction Fe on M1 site
Muscovite	Ms	McMullin et al. (1991)	Activity coefficient from Chatterjee and Froese (1975)
Paragonite	Pg	McMullin et al. (1991)	Activity coefficient from Chatterjee and Froese (1975)
Plagioclase	Pl	Fuhrman and Lindsley (1988)	
Rutile	Rt	$a_{TiO_2,Rt} = X_{TiO_2,Rt}$	$X_{TiO_2,Rt}$ = Ti/(sum of all cations)
Titanite	Ttn	$a_{CaTiSiO_5,Ttn} = (Ca)(Ti)$	Ca, Ti are moles per 1 Si

Table 14. Estimates of temperature (T), pressure (P), and X_{CO_2}

Sample	Zone	Distance[a] (km)	T (°C)	P (kb)	X_{CO_2}	Reactions	Comments
JAW-197A-2	Ank–Ab	2.70	420[b]	7.00	0.016	1	P from 197A-3
JAW-197A-3	Ank–Ab	2.70	420[b]	7.00[c]	0.011	1, 2	
Wep-29a	Ank–Ol	1.32	500[b]	7.44[b]	0.028	1	
JAW-171A	Bt	0.00	577[b]	8.26[c]	0.322	3, 5	
JAW-179B	Bt	1.16	510[b]	7.14	0.070	5	P from 179H
JAW-179H	Bt	1.16	510[b]	7.14[c]	0.070	4, 5	
JvH-W-28-1	Bt	0.60	542[b]	7.67[c]	0.138	3, 5	
JvH-W-28-3	Bt	0.60	542[b]	7.60	0.137	3	Average P from 28-1 and 28-4
JvH-W-28-4	Bt	0.60	542[b]	7.53[c]	0.145	3, 5	
JAW-181B-2	Amp-I	1.06	515[b]	7.00	0.098	7	P from FF-2, H-1, SI
JAW-181F-3	Amp-I	1.06	515[b]	7.00	0.105	5	P from FF-2, H-1, SI
JAW-181FF-2	Amp-I	1.06	515[b]	7.00[c]	0.108	5, 7	
JAW-181H-1	Amp-I	1.06	515[b]	7.00[c]	0.104	6, 9	
JAW-181SI	Amp-I	1.06	515[b]	7.00[c]	0.099	6	
JAW-181SIV	Amp-I	1.06	515[e]	7.00	–	12	P from FF-2, H-1, SI
W-5	Amp-II	–2.93	607[d]	9.42[d]	0.550	5, 6, 9, 13	
W-6A	Amp-II	–2.93	608[d]	9.32[d]	0.560	5, 6, 9	
JAW-113D	Amp-II	–2.93	630[e]	9.90[e]	–	13, 14, 15	
JAW-163IR	Di-I	0.03	575[b]	8.08[b]	0.032	11	
JAW-163IIIH	Di-I	0.03	575[b]	8.08[b]	0.043	7	Amphibole rims
JAW-163IVA	Di-I	0.03	575[b]	8.08[b]	0.031	11	
JAW-170A	Di-I	–1.25	610[b]	8.03[c]	0.103	5, 7	
JAW-170C	Di-I	–1.25	610[b]	8.03	0.120	11	P from 170 A
JAW-14-2	Di-II	–1.29	610[b]	8.80[e]	–	16, 17	Geobarometer of Kohn and Spear (1990)
JAW-167A	Di-II	–2.83	610[b]	9.49[b]	0.075	11	
JAW-167D	Di-II	–2.83	610[b]	9.49[b]	0.077	11	
JAW-187A-2	Di-II	–2.28	596[d]	9.70[d]	0.050	6, 9, 11, 12	
JAW-187M-1	Di-II	–2.28	596	9.70	0.049	11	P, T from 187A-2
JAW-187N-3	Di-II	–2.28	596	9.70	0.054	11	P, T from 187A-2
JAW/JvH-CL	Di-II	–2.42	605[e]	8.87[e]	–	12, 13	

[a]Distance measured perpendicular to boundary between metapelitic biotite–garnet and staurolite–kyanite zones (cf. Ague 1994)
[b]T and/or P estimated from best-fit metamorphic field gradients
[c]P at which two reactions intersect in $T - X_{CO_2}$ space for the estimated T
[d]P, T, X_{CO_2} estimated by optimizing convergence of all reactions (linearly independent and dependent) to a single $P - T - X_{CO_2}$ region
[e]T and/or P computed using geothermobarometry reactions

imaging of sample Wep-8a indicates abundant prograde amphibole, but the prograde Kfs predicted by reaction 7 is absent from the interior of the metacarbonate layer. Traces of Kfs are present, but these are associated with Bt (often partially chloritized) and Fe-oxides, implying retrograde reactions that broke down Bt and produced Kfs, Fe-oxide, and chlorite. Consequently, amphibole formation almost certainly occurred via dolomite breakdown (e.g. reaction 8 in Table 2). The magnitude of the gradients in X_{CO_2} that existed across this layer may have been smaller than previously inferred because the interior of the layer lacks a prograde mineral assemblage suitable for estimation of X_{CO_2}.

Oxygen fugacity and fluid composition

These calculations assumed graphite saturation because metamorphosed organic matter is ubiquitous throughout the Wepawaug Schist. For each sample, the oxygen fugacity (f_{O_2}) was adjusted to yield the X_{CO_2} value estimated for the sample. The estimated f_{O_2} values are relatively low, within about ± 0.6 log units of the quartz–fayalite–magnetite buffer. Estimated mole fractions of reduced species (e.g., CH_4, CO, H_2) are small, $< 10^{-2}$, similar to the results of Ferry (1992) for rocks elsewhere in New England. If the graphite was kinetically limited from reaction, then the f_{O_2} values would have likely been higher, and the mole fractions of the reduced species even smaller.

Magnitude of concentration gradients needed for prograde CO_2 loss

The model advanced by Hewitt (1973) drives prograde reaction and CO_2 loss from the metacarbonate layers in response to infiltration of H_2O from the surroundings. Regional advection probably occurred mostly along layers and through fractures (cf. Palin 1992; Ague 1994, 2000; Ferry 1994), although the regular zonal sequence of mineral assemblages observed at many lithologic contacts and in reaction selvages around veins implies that transport by diffusion across layers and away from conduits also occurred (e.g., Hewitt 1973; Vidale and Hewitt 1973), probably augmented by me-

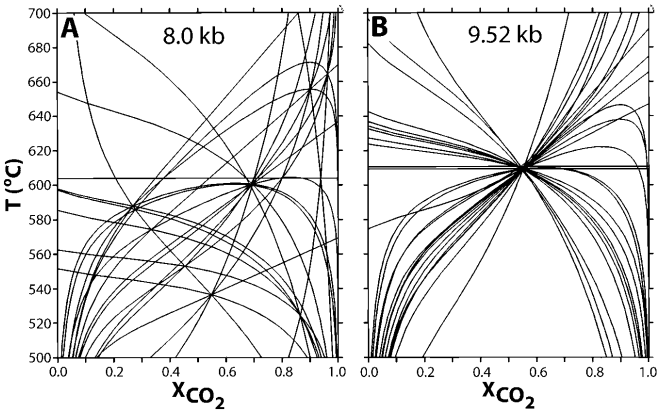

Fig. 3A,B. Temperature X_{CO_2} diagrams for sample W-5 illustrating technique for estimating equilibration pressure. **A** At 8 kb, the reactions do not converge. **B** At 9.52 kb, all reactions converge to a small region in $P - T - X_{CO_2}$ space; this pressure is taken as the best estimate for the rock

chanical dispersion and some cross layer advection (Ague 2000). This cross layer transport of H_2O into, and CO_2 out of, the metacarbonate layers can account for much of the observed prograde reaction, and is discussed in detail by Ague and Rye (1999) and Ague (2000). The H_2O could have come from local dehydrating schists (e.g., Hewitt 1973; Ague and Rye 1999; Ague 2000), or some source external to the metasedimentary rocks (e.g., Tracy et al. 1983; Palin 1992; Ague and Rye 1999).

Hewitt postulated that steep concentration gradients drove diffusion (see Fig. 6 in Hewitt 1973). However, the results of this study, as well as those from numerical models (Ague and Rye 1999; Ague 2000), strongly suggest that the change in X_{CO_2} across contacts and vein selvages may have often been very small– less than ~0.02. Flow of cooling fluid "down-T" will tend to drive retrograde reaction that puts CO_2 into rocks rather than removing it (e.g., Baumgartner and Ferry 1991; Ague 2000). Because it is likely that fluids were ascending and cooling through the metasedimentary sequence, at least in the amphibolite and upper greenschist facies (Ague 1994), the magnitude of the concentration gradients needed to drive diffusion/mechanical dispersion across layers must have been large enough to overcome the effects of down-T flow. This section explores steady-state analytical solutions to the advection–dispersion-reaction equation to determine the magnitude of local concentration gradients across layers needed to drive prograde reaction and CO_2 loss in a flow field where fluids are ascending and cooling at the regional scale.

Conservation of mass for fluid species i (e.g., CO_2, H_2O) in a reacting porous medium is given by (cf. Bear 1972; Garven and Freeze 1984; Ague and Rye 1999; Ague 2000):

$$\frac{\partial(\phi C_i)}{\partial t} = \nabla \cdot \left(\phi \overline{\overline{D_i}} \nabla C_i\right) - \nabla \cdot \left(\vec{q} C_i\right) + \phi \sum_j R_{i,j} \qquad (1)$$

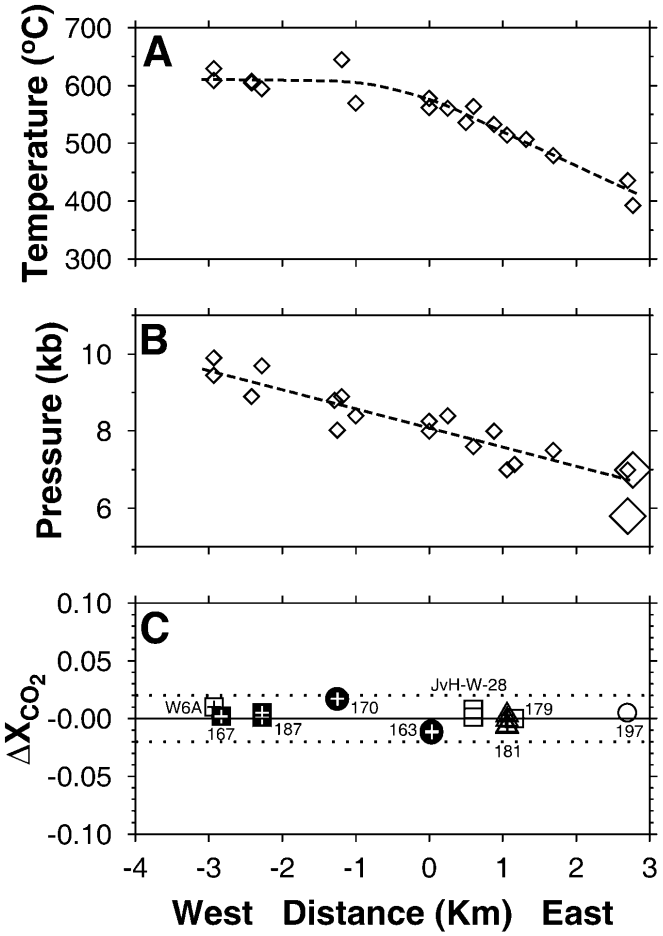

Fig. 4A–C. Regional profiles. **A** Estimated peak temperature and **B** pressure. Distances are measured perpendicular to the boundary between the metapelitic Bt–Grt and St–Ky zones following Ague (1994). Includes estimates from Tables 3 and 14 of this paper; for samples 35B, 49, 99A, 113D, 114A, 125Aii, and 131A from Ague (1994); and for sample MBW-1 from van Haren et al. (1996). Garnet data from Ague (1994) for 113D modified as described in the text. Distances for calcite–dolomite thermometry samples 133, 168K, 190B, and Wep-19a are 2.70, 2.70, 2.77, and 0.50 km, respectively (Table 3). Multiple estimates for a given locality were averaged for plotting and for least-squares fits. Greenschist facies samples plot between 0 and 3 km; amphibolite facies between –3 and 0 km. *Large diamonds* on pressure diagram correspond to minimum pressure estimates from phengite barometry (Massonne and Schreyer 1987) for samples 197A-3 and 198A. **C** Differences in estimated X_{CO_2} for metacarbonate layers. X_{CO_2} for layer margins, vein selvages, or calc-silicates subtracted from X_{CO_2} for layer interiors (ΔX_{CO_2}). None of the ΔX_{CO_2} values are large enough to be statistically significant (greater than ± 0.02). X_{CO_2} for JAW-163IIIH used to represent interior of JAW-163 layer. Sample localities and *symbols* as in Fig. 1B

in which C_i is the concentration of i, ϕ is porosity, t is time, $\overline{\overline{D_i}}$ is the hydrodynamic dispersion tensor for i, $\vec{q}$ is the Darcy flux vector, and $R_{i,j}$ is the production/consumption rate of i for reaction j. Hydrodynamic dispersion mass transfer by both mechanical dispersion and by diffusion of i through the fluid-filled porosity is denoted by the first term on the right-hand side; advective mass transfer is denoted by the second term;

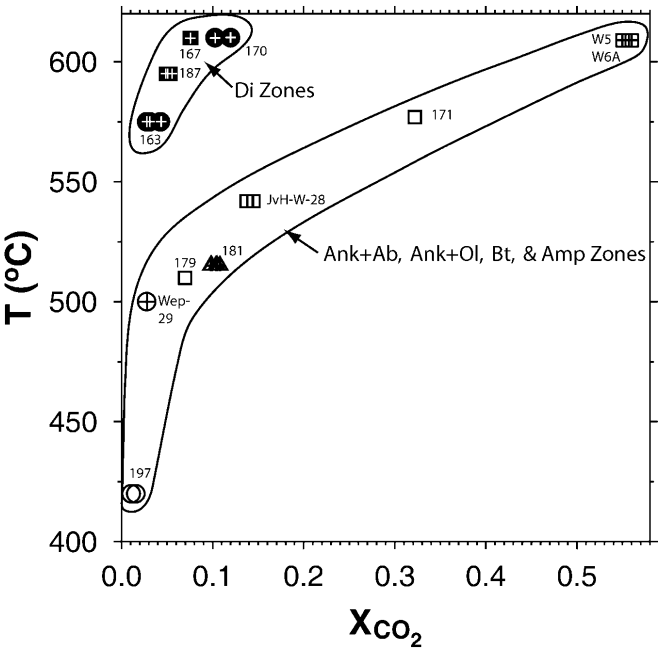

Fig. 5. Temperature-X_{CO_2} relations. Sample localities and *symbols* as in Fig. 1B. Note that X_{CO_2} estimates for a given layer are indistinguishable within uncertainty regardless of sample position within the layer

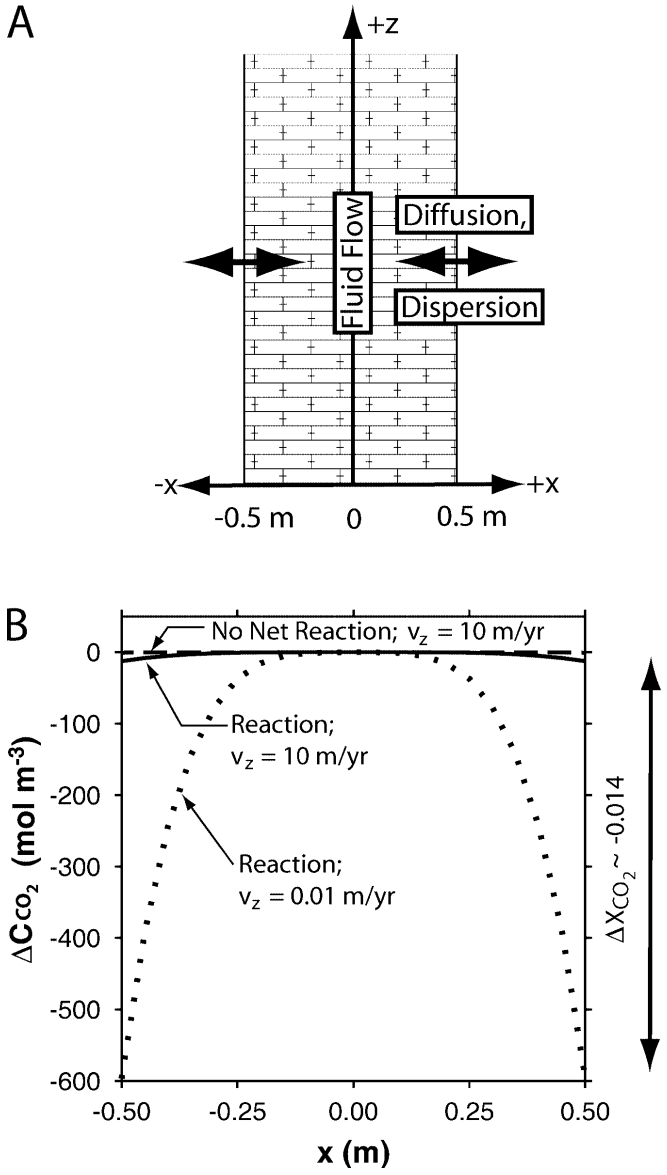

Fig. 6A,B. Analytical solutions to the advection–dispersion-reaction equation. **A** A 1-m-thick model metacarbonate layer (*brick pattern*). Regional fluid flow is parallel to z; diffusion and mechanical dispersion occur parallel to x and perpendicular to lithologic contacts. Temperature and pressure decrease in the direction of flow (positive z direction). **B** Concentration gradients across layer. Flow is parallel to the z coordinate axis, perpendicular to the x axis and the page. *Dashed line* results from Eq. (6) for no net reaction; *dotted* and *solid lines* results from Eq. (8) with reaction and CO_2 loss from the layer for flow velocities of 0.01 and 10 m year^{-1}

and mass changes because of chemical reaction are denoted by the third term. The following analysis is two-dimensional and focuses on a model metacarbonate layer, which runs parallel to the z coordinate axis and perpendicular to the x-axis (Fig. 6A). Advection is parallel to layering and z, whereas cross layer transport occurs parallel to x, relationships appropriate for the Wepawaug Schist (Ague 2000). The mineral assemblage and mineral compositions are uniform throughout the layer, and one reaction proceeds ($j=1$). Concentration gradients because of T and P effects in the direction of flow are small, so hydrodynamic dispersion fluxes parallel to z are neglected (e.g., Ague 1998). With the above constraints, Eq. (1) reduces to:

$$\frac{\partial(\phi C_i)}{\partial t} = \frac{\partial(\phi D_i[\partial C_i/\partial x])}{\partial x} - \frac{\partial(q_z C_i)}{\partial z} + \phi R_i \tag{2}$$

in which D_i is the coefficient of hydrodynamic dispersion parallel to x and q_z is the Darcy flux parallel to z.

The Darcy flux, coefficient of hydrodynamic dispersion, and porosity were held fixed and did not vary as a function of x. Thus, at steady-state Eq. (2) becomes:

$$D_i\phi\frac{\partial^2 C_i}{\partial x^2} = q_z\frac{\partial C_i}{\partial z} + C_i\frac{\partial q_z}{\partial z} - \phi R_i \tag{3}$$

The $\partial C_i/\partial z$ term is simply the concentration gradient in the direction of flow. At steady-state far-removed from heterogeneities such as sharp geochemical fronts, the value of this gradient approaches that defined by local fluid–rock equilibrium, even when the C_i values themselves diverge from local equilibrium because of kinetic effects (cf. Fig. 10B in Ague 1998). Consequently, for specified T and P gradients, we can write:

$$G_i^* = \frac{\partial C_i}{\partial z} = \frac{\partial C_i}{\partial T}\frac{\partial T}{\partial z} + \frac{\partial C_i}{\partial P}\frac{\partial P}{\partial z} \tag{4}$$

in which $\partial C_i/\partial T$ and $\partial C_i/\partial P$ are given by local fluid–rock equilibrium. The common reactions that produced index minerals in the Wepawaug Schist are dominated by positive $\partial C_{CO_2}/\partial T$ in the fluid composition range of

interest (cf. Ague and Rye 1999). A typical $G^*_{CO_2}$ value for such reactions is –2 mol m^{-3} (fluid) m^{-1} for a representative geothermal gradient of –20 °C km^{-1} (T decreases upward) and the lithostatic pressure gradient of –0.28 bar m^{-1}. This regional $G^*_{CO_2}$ was used in all calculations below, is fully consistent with the positive $T - X_{CO_2}$ trend defined by Wep-29, 179, 181, JvH-W-28, 171, and W5/W6 (Fig. 5), and approximates the largest (absolute value) regional gradient due to T and P effects likely for the Wepawaug Schist.

The hydrodynamic dispersion coefficient is (cf. Bear 1972):

$$D_i = \alpha_{T,i}\left|\frac{q_z}{\phi}\right| + D_{f,i}\tau \tag{5}$$

in which $\alpha_{T,i}$ is the transverse dispersivity, τ is the tortuosity parallel to x, and $D_{f,i}$ is the diffusion coefficient for i. Values used for the model were $\alpha_{T,i} = 0.5$ m, $\phi = 10^{-3}$, $\tau = 0.3$, and $D_{f,i} = 10^{-8}$ m^2 s^{-1} (Ague 2000). These values are representative; others change the details of the results but do not affect the conclusions of this study.

The concentration profile across a model metacarbonate layer at any given elevation is symmetrical for the simple system herein. To release CO_2 with prograde reaction during down-T flow, C_{CO_2} must be smallest at the layer edges and rise to a global maximum at the center of the layer (cf. Ague and Rye 1999; Ague 2000). C_{H_2O} does the opposite, reaching a global minimum in the center. Thus, at the center of a layer ($x = 0$), we have the boundary condition that $\partial C_i/\partial x = 0$ (Fig. 6B). The simplest solution to Eq. (3) is one where the effects of cross layer hydrodynamic dispersion precisely balance those of down-T flow such that no net reaction occurs ($R_i = 0$ and $\partial q_z/\partial z$ is negligible). Integration of Eq. (3) twice subject to the above constraints gives:

$$\Delta C_i = C_i^x - C_i^{x=0} = \frac{q_z G_i^* x^2}{2D_i\phi} = \frac{v_z G_i^* x^2}{2D_i} \tag{6}$$

in which ΔC_i is the difference in concentration between position x and $x = 0$, C_i^x and $C_i^{x=0}$ are the concentrations of i at x and $x = 0$, respectively, and v_z is the pore fluid velocity ($v_z = q_z/\phi$). Equation (6) indicates that the concentration profiles will be parabolic. The examples below consider a representative system with $X_{CO_2} = 0.1$ at the center of the model layer, $T = 550$ °C, and $P = 8$ kb.

Calculated C_{CO2} profiles across a 1-m-thick layer are shown in Fig. 6B for a large pore fluid velocity of 10 m $year^{-1}$. The boundaries at $x = \pm 0.5$ m could represent "contacts" with dehydrating schists or with quartz veins. The results give the minimum difference in concentration between the center and the edges of the layer needed for prograde CO_2 loss. The lateral concentration gradients act to remove CO_2 from the rock and drive prograde reaction whereas the down-T advective flux acts to add CO_2 and drive retrogression. Fluid composition changes across the layer are remarkably small (Fig. 6B). Even for the large down-T flow velocity of 10 m $year^{-1}$, the difference in X_{CO_2} across the layer is only $\sim 10^{-5}$. Gradients in fluid composition would be even smaller if the pore fluid velocity was smaller.

If CO_2 is produced by typical devolatilization reactions, then R_{CO_2} and $\partial q_z/\partial z$ are nonzero. The magnitudes of concentration gradients perpendicular to flow must increase relative to the no reaction case in order to increase hydrodynamic dispersion fluxes and keep the system at steady-state. For the exploratory purposes of this study, it was found adequate to neglect the $\partial q_z/\partial z$ term because it has considerably less impact on concentration gradients than the reaction term. In general, reaction rates will be greatest near layer edges, and decrease inward (e.g., Ague and Rye 1999). Thus, the rate expression $\phi R_i = \phi r_i x^2$ was used, in which r_i is a constant; other simple rate expressions yield comparable results. Integration of Eq. (3) yields:

$$\frac{\partial C_i}{\partial x} = \frac{v_z G^* x}{D_i} - \frac{r_i x^3}{3D_i} \tag{7}$$

and

$$\Delta C_i = C_i^x - C_i^{x=0} = \frac{v_z G^* x^2}{2D_i} - \frac{r_i x^4}{12D_i} \tag{8}$$

Progressive metamorphism to diopside zone conditions in the Wepawaug Schist resulted in the loss of roughly 15 g CO_2 per 100 g initial rock. Consider an average CO_2 production rate large enough to release this CO_2 in just 10^4 model years (3.02×10^{-8} mol m^{-3} (rock) s^{-1}). The value of the rate constant r_{CO_2} can be found using the definition of the average of a function:

$$\text{Average rate} = 3.02\times10^{-8} = \frac{\phi r_{CO_2}\int_{-0.5}^{0.5} x^2 dx}{0.5-(-0.5)} = 8.33\times10^{-5} r_{CO_2} \tag{9}$$

which yields $r_{CO_2} = 3.62\times10^{-4}$ for a 1-m-thick layer. Even with this extremely large CO_2 production rate, concentration gradients are still very small and amount to X_{CO_2} differences of only 0.014 across the layer for the small down-T flow velocity of 0.01 m $year^{-1}$ (Fig. 6B). Reaction could be further enhanced if a component of cross layer advection augmented the hydrodynamic dispersion (not modeled). At the edges of the layer ($x = \pm 0.5$ m), the absolute value of the concentration gradient from Eq. (7) is ~4,800 mol m^{-3} (fluid) m^{-1}, which clearly dominates the regional gradient parallel to flow of –2 mol m^{-3} (fluid) m^{-1}. Increases in velocity increase the value of D_i [Eq. (5)] and, thus, the rate of cross layer mass transfer. These effects decrease the magnitudes of the reaction term in Eq. (8) and the cross layer concentration gradients (Fig. 6B). Increasing the time of reaction decreases the gradients needed for CO_2 loss; X_{CO_2} differences across the layer are reduced to just $\sim 10^{-4}$ for $v_z = 0.01$ m $year^{-1}$ if the time

scale of the reaction is increased to 10^6 years (not illustrated).

Equations (7) and (8) hold that the CO_2 produced is transported parallel to x out of the layer by hydrodynamic dispersion. If the $\partial q_z/\partial z$ term was included in the analysis, some of the CO_2 produced would be transported along z by advection, and it is easily shown from Eq. (3) that concentration gradients parallel to x would be slightly smaller than those in Fig. 6B for the water-rich fluids considered.

The small concentration gradients across layers predicted by Eqs. (6) (7) and (8) are consistent with the results of numerical modeling (Ague 2000), and are clearly far too small to be resolved by current field-based methods. Therefore, it is important to emphasize that although no large gradients in X_{CO_2} across layers were observed (Figs. 4C and 5), the differences in X_{CO_2} could have been much smaller than the resolvable limit of $\sim$0.02 and still have driven prograde reaction and CO_2 loss, even in the presence of strong down-T advection.

Equation (8) can also be used to investigate time scales of reaction for large differences in fluid composition across layers. For example, if X_{CO_2} was 0.1 in the center of the layer and 0.05 at the edges, $\Delta C_{CO_2} = -2,232$ mol m^{-3}. With all other conditions being the same as in previous reaction examples, the r_{CO_2} values derived from Eq. (8) suggest that the approximate time scales needed for release of 15 wt% CO_2 are only $\sim$3,000 and $\sim$50 years for v_z of 0.01 and 10 m year^{-1}, respectively. The implication is that large gradients in H_2O–CO_2 fluid composition will tend to be eliminated over short time scales of fluid–rock interaction.

The diopside zones

The mineral assemblages of the diopside zones are stable at high T ($>\sim$575 °C) and relatively low X_{CO_2} (Fig. 5). Similar low X_{CO_2} fluids have been observed in diopside zones elsewhere in New England (e.g., Ferry 1992; Léger and Ferry 1993), and could arise in two main ways. (1) When the reactants needed to produce biotite and amphibole are exhausted, the rocks would lose their ''buffer capacity'' and would no longer be producing CO_2. X_{CO_2} could then drop due to infiltration of water from surrounding schists that continue to dehydrate during heating (cf. Hewitt 1973; Ague and Rye 1999). (2) X_{CO_2} could decrease because of advection-driven infiltration of a water-rich fluid external to the metasedimentary sequence.

The low X_{CO_2} fluid of the Diopside zones was present at peak P–T conditions that are indistinguishable from those of the immediately adjacent zones, implying that P and T were not the main variables controlling the formation of the diopside zones. Oxygen isotope evidence indicates that the diopside zones were infiltrated, at least in part, by external fluids as much as several per mil lighter than the metasediments (Tracy et al. 1983; Palin 1992; van Haren et al. 1996). Thus, it is probable that the low X_{CO_2} of the diopside zones arose when the regional metapelite dehydration flux was augmented by an external, water-rich fluid from an isotopically light reservoir. The external fluids flowed along contacts, through fractures, and pervasively along grain boundaries. Two possibilities exist for the external reservoir (Palin 1992; van Haren et al. 1996). The first is fluids equilibrated with or evolved from the syn-metamorphic magmas that intruded the high-grade parts of the Wepawaug Schist. van Haren et al. (1996) found that the oxygen isotope signature of these magmas was consistent with that of the isotopically light fluids that infiltrated the diopside zones. The second possible source is dehydration of the mafic metavolcanic rocks that underlie the sequence (cf. Fritts 1965). Of the two possible sources, ''magmatic'' fluids are perhaps more likely because of the close spatial association of the diopside zones and the syn-metamorphic intrusions, although some contribution from dehydration of the underlying mafic metavolcanics cannot be ruled out. Magmatic fluids are also thought to have been important during diopside zone metamorphism in northern New England (Ferry 1992; Léger and Ferry 1993).

Discussion and conclusions

Water derived from dehydrating schists or external fluid sources that is transported into metacarbonate layers across lithologic contacts or vein selvages can drive prograde reaction and CO_2 loss, but this process requires that concentration gradients in fluid composition be present during reaction (Hewitt 1973; Ague and Rye 1999; Ague 2000). For the samples of this study, large gradients in X_{CO_2} either did not exist or were not recorded across metacarbonate layers or in reaction selvages around syn-metamorphic veins. However, analytical solutions to the two-dimensional advection–dispersion-reaction equation indicate that gradients in fluid composition could have been extremely small and yet still have been adequate to drive prograde CO_2 loss by hydrodynamic dispersion in a flow field. It is concluded that current methods for estimating X_{CO_2} in fluids based on the compositions of coexisting minerals are not precise enough to resolve the small gradients across layers that probably existed during much of the metamorphism.

Fluid exchange between devolatilizing schists and metacarbonate rocks across contacts and vein selvages (Hewitt 1973; Ague and Rye 1999; Ague 2000) is thought to have driven much of the devolatilization in the greenschist and parts of the amphibolite facies (ankerite–oligoclase, biotite, and at least part of the amphibole zones). At the highest metamorphic grades, the rocks could have lost their ability to maintain X_{CO_2} at high values because of consumption of reactants needed to produce biotite and amphibole. H_2O input

from dehydrating schists would have then caused X_{CO_2} to drop toward the low values needed for diopside zone conditions. However, the isotopically light oxygen of the diopside zones suggests that the regional dehydration flux of H_2O derived from schists was augmented by another H_2O source flowing at the regional scale (Tracy et al. 1983; Palin 1992; van Haren et al. 1996). Fluids either evolved from or equilibrated with syn-metamorphic igneous intrusions are considered the most likely source, although dehydration waters derived from underlying mafic metavolcanic rocks may have also played a role (Palin 1992; van Haren et al. 1996).

Large gradients in H_2O–CO_2 fluid composition possibly existed across some layers and vein selvages. However, the models of this study indicate that large gradients lead to fast reaction rates that can, in turn, wipe the gradients out over time scales of fluid–rock interaction perhaps as short as 10^2–10^4 years. Oxygen isotope studies indicate that such short time scales of fluid–rock interaction are possible (Palin 1992; van Haren et al. 1996). In summary, large gradients across a given layer would tend to be rapidly eliminated and, hence, rarely preserved in the rock record.

Acknowledgements I thank E.W. Bolton, C.J. Carson, J.O. Eckert Jr., J.M. Ferry, J.M. Palin, S. Penniston-Dorland, D.M. Rye, J.L.M. van Haren, and B.A. Wing for discussions, the South Central Connecticut Regional Water Authority for outcrop access, and C.P. Chamberlain and an anonymous referee for reviews. Financial support from National Science Foundation grants EAR-9706638 and EAR-9810089 is gratefully acknowledged.

References

Ague JJ (1994) Mass transfer during Barrovian Metamorphism of Pelites, south-central Connecticut, II: channelized fluid flow and the growth of staurolite and kyanite. Am J Sci 294:1061–1134

Ague JJ (1998) Simple models of coupled fluid infiltration and redox reactions in the crust. Contrib Mineral Petrol 132:180–197

Ague JJ (2000) Release of CO_2 from carbonate rocks during regional metamorphism of lithologically heterogeneous crust. Geology 28:1123–1126

Ague JJ, Rye D M (1999) Simple models of CO_2 release from metacarbonates with implications for interpretation of directions and magnitudes of fluid flow in the deep crust. J Petrol 40:1443–1462

Ague JJ, van Haren JLM (1996) Assessing metasomatic mass and volume changes using the bootstrap, with application to deep-crustal hydrothermal alteration of marble. Econ Geol 91:1169–1182

Ague JJ, Baxter EF, Eckert JO Jr (2001) High f_{O2} during sillimanite zone metamorphism of part of the Barrovian type locality, Scotland. J Petrol 42:1301–1320

Anovitz LM, Essene EJ (1987) Phase equilibria in the system $CaCO_3$–$MgCO_3$–$FeCO_3$. J Petrol 28:389–414

Bahr JM (1976) Structure and petrology of the Woodbridge granite. BSc Thesis, Yale University, New Haven

Baumgartner LP, Ferry JM (1991) A model for coupled fluid-flow and mixed-volatile mineral reactions with applications to regional metamorphism. Contrib Mineral Petrol 106:273–285

Bear J (1972) Dynamics of fluids in porous media. Elsevier, New York

Berman RG (1990) Mixing properties of Ca–Mg–Fe–Mn garnets. Am Mineral 75:328–344

Berman RG (1991) Thermobarometry using multi-equilibrium calculations: a new technique, with petrological applications. Can Mineral 29:833–855

Berman RG, Aranovich LY (1996) Optimized standard state and solution properties of minerals I. Model calibration for olivine, orthopyroxene, cordierite, garnet, and ilmenite in the system FeO–MgO–CaO–Al_2O_3–TiO_2–SiO_2. Contrib Mineral Petrol 126:1–24.

Blundy JD, Holland TJB (1990) Calcic amphibole equilibria and a new amphibole–plagioclase geothermometer. Contrib Mineral Petrol 104:208–224

Chatterjee ND, Froese E (1975) A thermodynamic study of the pseudobinary join muscovite-paragonite in the system KalSi_3O_8–$NaAlSi_3O_8$–Al_2O_3–SiO_2–H_2O. Am Mineral 60:985–993

Deer WA, Howie, RA, Zussman J (1992) An introduction to the rock-forming minerals. Longman, New York

Efron B, Tibshirani RJ (1993) An introduction to the bootstrap. Chapman and Hall, New York

Ferry JM (1992) Regional metamorphism of the Waits River Formation, eastern Vermont: delineation of a new type of giant metamorphic hydrothermal system. J Petrol 33:45–94

Ferry JM (1994) Overview of the petrologic record of fluid flow during regional metamorphism in northern New England. Am J Sci 294:905–988

Fritts CE (1965) Bedrock geologic map of the Ansonia quadrangle, Fairfield and New Haven Counties, Connecticut. US Geological Survey Quadrangle Map GQ-426

Fuhrman ML, Lindsley DH (1988) Ternary feldspar modelling and thermometry. Am Mineral 73:201–215

Garven G, Freeze RA (1984) Theoretical analysis of the role of groundwater flow in the genesis of stratabound ore deposits. 1. Mathematical and numerical model. Am J Sci 284:1085–1124

Hewitt DA (1973) The metamorphism of micaceous limestones from south-central Connecticut. Am J Sci 273-A:444–469

Holland TJB, Blundy J (1994) Non-ideal interactions in calcic amphiboles and their bearing on amphibole–plagioclase thermometry. Contrib Mineral Petrol 116:433–447

Holland TJB, Powell R (1990) An enlarged and updated internally consistent thermodynamic dataset with uncertainties and correlations: the system K_2O–Na_2O–CaO–MgO–MnO–FeO–Fe_2O_3–Al_2O_3–TiO_2–SiO_2–C–H_2–O_2. J Metamorph Geol 8:89–124

Kerrick DM, Jacobs GK (1981) A modified Redlich–Kwong equation for H_2O, CO_2, and H_2O–CO_2 mixtures at elevated temperatures and pressures. Am J Sci 281:735–767

Kohn MJ, Spear FS (1990) Two new geobarometers for garnet amphibolites, with application to southeastern Vermont. Am Mineral 75:89–96

Kohn MJ, Spear FS (2000) Retrograde net transfer reaction insurance for pressure–temperature estimates. Geology 28:1127–1130

Kretz R (1983) Symbols for rock-forming minerals. Am Mineral 68:277–279

Lanzirotti A, Hanson GN (1996) Geochronology and geochemistry of multiple generations of monazite from the Wepawaug Schist, Connecticut, USA: implications for monazite stability in metamorphic rocks. Contrib Mineral Petrol 125:332–340

Léger A, Ferry JM (1993) Fluid infiltration and regional metamorphism of the Waits River Formation, northeast Vermont, USA. J Metamorph Geol 11:3–29

Mäder UK, Percival JA, Berman RG (1994) Thermobarometry of garnet–clinopyroxene–hornblende granulites from the Kapuskasing structural zone. Can J Earth Sci 31:1134–1145

Massonne H, Schreyer W (1987) Phengite geobarometry based on the limiting assemblage with K-feldspar, phlogopite, and quartz. Contrib Mineral Petrol 96:212–224.

McMullin DWA, Berman RG, Greenwood HJ (1991) Calibration of the SGAM thermobarometer for pelitic rocks using data from phase-equilibrium experiments and natural assemblages. Can Mineral 29:889–908

Palin JM (1992) Stable isotope studies of regional metamorphism in the Wepawaug Schist, Connecticut. PhD Thesis, Yale University, New Haven

Smith JV, Brown WL (1988) Feldspar minerals 1. Springer, New York

Tracy RJ, Rye DM, Hewitt DA, Schiffries CM (1983) Petrologic and stable-isotopic studies of fluid–rock interactions, south-central Connecticut: I. the role of infiltration in producing reaction assemblages in impure marbles. Am J Sci 283-A:589–616

van Haren JLM, Ague JJ, Rye DM (1996) Oxygen isotope record of fluid infiltration and mass transfer during regional metamorphism of pelitic schist, south-central Connecticut, USA. Geochim Cosmochim Acta 60:3487–3504

Vidale RJ, Hewitt DA (1973) ''Mobile'' components in the formation of calc-silicate bands. Am Mineral 58:991–997